nature cell biology

Article

https://doi.org/10.1038/s41556-024-01532-6

Differential stiffness between brain vasculature and parenchyma promotes metastatic infiltration through vessel co-option

Received: 23 September 2023

Accepted: 18 September 2024

Published online: 24 October 2024

Check for updates

Marina Uroz[1,2,3], Amy E. Stoddard[1,2,3,4], Bryan P. Sutherland[1,2,3], Olivia Courbot[5,6], Roger Oria[7,8], Linqing Li[1,2,3,9], Cara R. Ravasio[1], Mai T. Ngo[1,2,3], Jinling Yang[1,2,3], Juliann B. Tefft[1,2,3], Jeroen Eyckmans[1,2,3], Xue Han[1], Alberto Elosegui-Artola[5,6], Valerie M. Weaver[7,8,10,11] & Christopher S. Chen[1,2,3]

In brain metastasis, cancer cells remain in close contact with the existing vasculature and can use vessels as migratory paths—a process known as vessel co-option. However, the mechanisms regulating this form of migration are poorly understood. Here we use ex vivo brain slices and an organotypic in vitro model for vessel co-option to show that cancer cell invasion along brain vasculature is driven by the difference in stiffness between vessels and the brain parenchyma. Imaging analysis indicated that cells move along the basal surface of vessels by adhering to the basement membrane extracellular matrix. We further show that vessel co-option is enhanced by both the stiffness of brain vasculature, which reinforces focal adhesions through a talin-dependent mechanism, and the softness of the surrounding environment that permits cellular movement. Our work reveals a mechanosensing mechanism that guides cell migration in response to the tissue's intrinsic mechanical heterogeneity, with implications in cancer invasion and metastasis.

The ability of cancer cells to migrate and disseminate within tissues is one of the hallmarks of metastasis and is associated with a poor prognosis. Although metastatic cell migration in tissues can be random and isotropic, it is often directionally guided by topology[1] and follows areas of bundled or aligned extracellular matrix (ECM) fibres[2–5] or pre-existing structures such as nerves[6,7], muscle fibres[7,8] or blood vessels[9–18]. In the brain, metastatic cells from melanoma, breast or lung cancer often remain in close contact with the vasculature after extravasation. Instead of detaching from vessels and invading the brain parenchyma, metastatic cells use blood vessels as paths for migration co-opting the existing brain vasculature[10,11,16,18]. While previous studies have shown that the attachment and spreading of metastatic cells along the basal side of blood vessels is necessary for their survival and proliferation in the brain[11,16], the mechanisms driving cancer cell migration along the vasculature remain poorly understood.

It has previously been shown that metastatic cells can adhere to the vascular basement membrane ECM through focal adhesions[10] and that the adhesive and mechanical properties of the ECM are critical regulators of cell migration[19]. Specific ECM components and matrix rigidity affect integrin engagement, influencing adhesion and migration phenotypes[20,21]. Compared with other organs, the brain is mechanically soft, and the parenchymal ECM primarily consists of glycosaminoglycans (such as hyaluronic acid (HA)) and proteoglycans[22]. The concentration of the classically more adhesive, fibrous ECM proteins

A full list of affiliations appears at the end of the paper. e-mail: chencs@bu.edu

(such as collagens or fibronectin) is low and mainly present at the basement membrane of blood vessels[23]. Despite the importance of the adhesive and mechanical properties of the extracellular environment in cell migration, whether the unique mechanical properties of the brain drive metastatic invasion along the vasculature remains unresolved.

Here, we show that not only metastatic cells but adherent cells in general invade brain tissue by migrating along vessels. Combining mouse brain slices and an engineered microvasculature device, we show that cells spread along the vascular basement membrane ECM and migrate using focal adhesions. Our data reveal that the extent of invasion not only is influenced by the difference in ECM composition between the vasculature and the brain parenchyma but is regulated by the relatively higher stiffness of the vasculature. This differential stiffness promotes brain invasion via vessel co-option through a talin-dependent mechanism.

Results

Adherent cells invade brain tissue via vascular migration

Because all metastatic cells start their journey into the brain in contact with the vasculature just after extravasation, it is difficult to determine relative propensity of cells to invade along vessels versus directly through brain tissue in an unbiased fashion. To address this, we seeded metastatic melanoma 1205Lu cells directly on top of 300-µm-thick mouse brain slices. This setup allows cells to initiate migration along any aspect of the tissue (Fig. 1a), facilitating the study of vessel co-option independently of extravasation. After 24 h of ex vivo culture, ~30–70% of the cells had adhered to the outer surface of the vasculature, while the rest remained in the bulk of the tissue (Extended Data Fig. 1a–c). The cells attached at these different locations within the tissue exhibited distinct cell shapes. Melanoma cells in the bulk remained round, whereas cells on vessels displayed a more elongated morphology, characterized by a significantly lower circularity (Fig. 1b,c). The cells in the bulk also appeared to be less motile compared with those able to migrate along the vasculature (Supplementary Video 1). To assess the invasion depth of melanoma cells into the brain slice after 4 and 24 h, we defined a reference at the top of the slice with confocal imaging and measured the depth of each cell into the slice (Extended Data Fig. 1d). The distributions of invasion depths showed that cells moving along vessels were able to penetrate much deeper into the slice, invading brain tissue more efficiently than cells moving through the bulk (Fig. 1b,d and Extended Data Fig. 1e,f).

To test whether this pattern of cell spreading and invasion along the vasculature was unique to metastatic melanoma cells, we tested ten other cell lines. First, we tested cancerous cell lines with different origins and metastatic potentials including melanoma cell lines (WM983B, A375P and A375M2), breast cancer cell lines (MCF7 and MDA-MB-231) and an osteosarcoma cell line (U2OS) (Fig. 1e). We also examined non-cancerous neonatal human dermal fibroblasts (nHDF), breast epithelial cells (MCF10A) and brain pericytes (human brain vascular pericytes, HBVPC) (Fig. 1f). Remarkably, for all these adherent cell types, the cells in the bulk were significantly rounder than on vessels (Fig. 1g–i), and they were able to migrate significantly deeper into the brain slice when following the vasculature (Fig. 1j–l and Extended Data Fig. 2a–f). Further, mouse-derived cells also showed similar trends (Extended Data Fig. 2g,h). Thus, vessel co-option is not a rare property of human metastatic cancer cells but rather a common capability amongst adherent cells. Only primary non-adherent immune cells (T cells) remained round, even in close proximity to vessels, and migrated through brain tissue without adhering to them (Extended Data Fig. 2i–k).

Talin-driven migration regulates vessel co-option

Based on these findings, we next investigated the contribution of cell–ECM adhesion to vessel co-option. Previous studies have shown that cells move along the basement membrane ECM and can adhere to it through focal adhesions[10,14]. By staining for phosphorylated paxillin, we observed focal adhesions primarily localized at the basement membrane of blood vessels, with some co-localizing with melanoma cell actin structures (Fig. 2a). The cells positioned at the brain–vessel interface are possibly interacting with both vascular basement membrane and brain ECM, so we tested the role of each of these interfaces. To target adhesion to HA, the main component of brain parenchymal ECM, we generated a clustered regularly interspaced short palindromic repeats (CRISPR)-mediated knockout (KO) of the HA adhesion receptor CD44 in the melanoma cell line and seeded them on brain slices (Extended Data Fig. 3a,b). CD44 is often overexpressed in glioblastoma and provides a mechanism for brain cancer cells to migrate through HA-rich environments independently of integrins[24–28]. In our system, KO of CD44 did not influence cell shape (Fig. 2b). Although the cells showed generally lower invasion depths both along vessels or through the bulk, the KO did not significantly block migration along vessels (Fig. 2c and Extended Data Fig. 3c,d), suggesting direct adhesion to HA is not essential for metastatic vessel co-option.

Next, we sought to target integrins, the primary receptors for ECM, which has been a prevailing strategy to block cancer cell migration[29,30]. However, cancer cells often express multiple integrins, making single integrin targeting less effective[14,31,32]. Indeed, in our system, while KO of integrin β1 reduced cell spreading along the basement membrane (Fig. 2d and Extended Data Fig. 3e,f), invasion into brain tissue by vessel co-option was not affected (Fig. 2e and Extended Data Fig. 3g,h). Given the redundancies of multiple integrins, we hypothesized that targeting focal adhesion adaptor proteins would be a more effective strategy to reduce invasion of the cancer cells along the vasculature, since adaptor proteins connect integrins to the cytoskeleton regardless of the integrin subtypes. To test this, we generated melanoma KO cell lines for zyxin, paxillin, talin 1 and talin 2 and assessed their cell shapes and invasion depths in brain slices (Extended Data Figs. 3i–m and 4a,b,f,g). For talin 1 and zyxin, KO cell lines were clonally derived (second clone in Extended Data Figs. 3 and 4). Knocking out paxillin, zyxin or talin 2 had no effect on cell shape or invasion depth (Fig. 2f,i,j,l and Extended Data Figs. 3n–q and 4h,i) nor did the inhibition of FAK using a small molecule compound, FC11 (Extended Data Fig. 3r–u). In contrast, talin 1-KO and talin 1 and talin 2 double-KO cells that adhered to the vasculature showed reduced cell spreading (Fig. 2g–i and Extended Data Fig. 4c) and a dramatic decrease in invasiveness into the tissue compared with controls (Fig. 2k,l and Extended Data Fig. 4d,e,h,i). Collectively, these results show that migration along the vasculature is focal adhesion-dependent and is regulated by the adaptor protein talin.

To validate these findings in vivo, we injected cells directly into brains of immunocompromised nu/nu mice. One week later, control tumours showed irregular boundaries, with cells clustered around and extending into the vasculature at the invasive front, a pattern that was disrupted in the KO tumours. Tumours from mice lacking both talin 1 and talin 2 exhibited instead reduced invasiveness, characterized by significantly smoother boundaries (Fig. 3a–c, Extended Data Fig. 5 and Supplementary Video 2).

Basement membrane ECM alone does not support vascular invasion

Given the role of focal adhesions in vessel co-option, we next asked whether the vascular basement membrane ECM is sufficient to drive metastatic elongation and invasion along vessels in the brain. To test this hypothesis, we seeded cancer cells on decellularized brain slices and investigated cell morphology and invasion depth 24 h later (Fig. 4a–d). Nuclear staining confirmed decellularization, while laminin staining demonstrated an intact vascular basement membrane (Fig. 4a). The cells preferentially adhered to the laminin-rich basement membrane and were able to spread along it, even in the absence of endothelial or neural cells (Fig. 4b,c). However, cells invaded less in decellularized brain slices than in intact brain slices and lost

https://doi.org/10.1038/s41556-024-01532-6

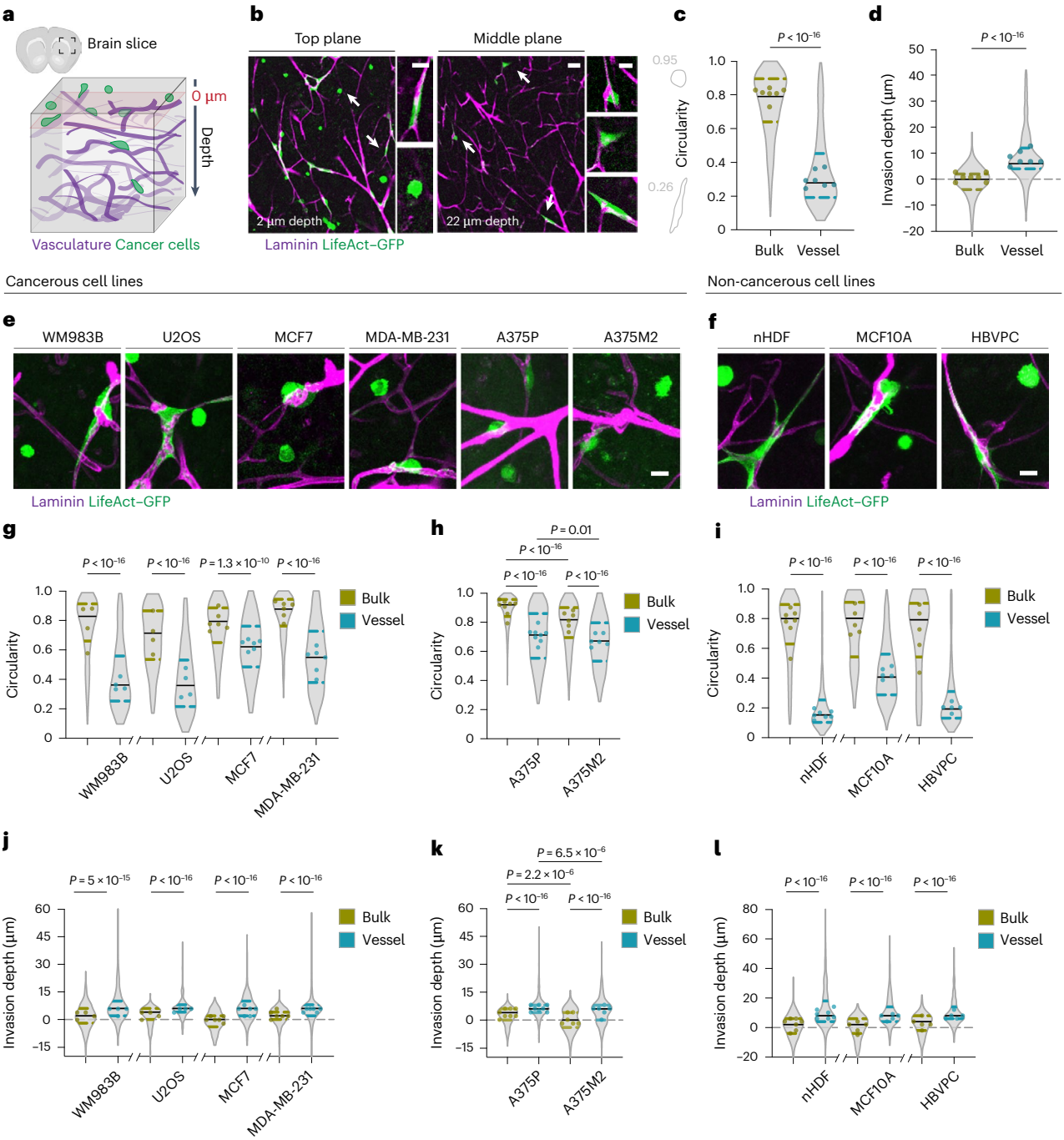

Fig. 1 | Adherent cells invade brain tissue by migrating along the vasculature. **a**, An illustration of the experimental model. **b**, A brain slice immunostaining of laminin (magenta) and 1205Lu LifeAct–GFP (green) at 2 µm (left) and 22 µm (right) below the top surface. The white arrows indicate zoomed-in cells. Scale bars, 50 µm and 20 µm (insets). The brain slice was created with BioRender.com. **c**, Violin plots of cell shape circularities for cells adhered to vessels or the bulk brain tissue 24 h after seeding. For reference, the contour and circularity of cells in **b**, top, are shown in grey. (**d**) Violin plots of invasion depths for cells adhered to vessels or the bulk brain tissue 24 h after seeding. **e**,**f**, A brain slice immunostaining of laminin (magenta) and LifeAct–GFP (green) (maximum projection, 24-µm-thick stack) of cancerous cell lines (WM983B, U2OS, MCF7, MDA-MB-231, A375P and A375M2) (**e**) and non-cancerous cell lines (nHDF, MCF10A and HBVPC) (**f**). Scale bar, 20 µm. **g**–**i**, Violin plots of cell shape circularities for cells on vessels or in the bulk for WM983B, U2OS, MCF7 and MDA-MB-231 (**g**); A375P and A375M2 (**h**); and nHDF, MCF10A and HBVPC (**i**). **j**–**l**, Violin plots of invasion depths for cells on vessels or in the bulk for WM983B, U2OS, MCF7 and MDA-MB-231 (**j**); A375P and A375M2 (**k**); and nHDF, MCF10A and HBVPC (**l**). For 1205Lu: $n = 463$ for bulk and $n = 584$ for vessel from seven slices and four experiments. For WM983B: $n = 295$ for bulk and $n = 254$ for vessel from four slices and four experiments. For U2OS: $n = 176$ for bulk and $n = 268$ for vessel from four slices and three experiments. For MCF7: $n = 146$ for bulk and $n = 223$ for vessel from six slices and three experiments. For MDA-MB-231: $n = 326$ for bulk and $n = 523$ for vessel from six slices and three experiments. For A375P: $n = 540$ for bulk and $n = 532$ for vessel from eight slices and four experiments. For A375M2: $n = 500$ for bulk and $n = 356$ for vessel from six slices and four experiments. For nHDF: $n = 382$ for bulk and $n = 651$ for vessel from seven slices and four experiments. For MCF10A: $n = 168$ for bulk and $n = 459$ for vessel from five slices and four experiments. For HBVPC: $n = 130$ for bulk and $n = 473$ for vessel from five slices and three experiments. The graphs show median ± interquartile range. The dots represent the medians per slice. For the statistical analysis, a two-sided Mann–Whitney or a Kruskal–Wallis test followed by a post hoc Dunn's test (for **h** and **k**) was performed.

https://doi.org/10.1038/s41556-024-01532-6

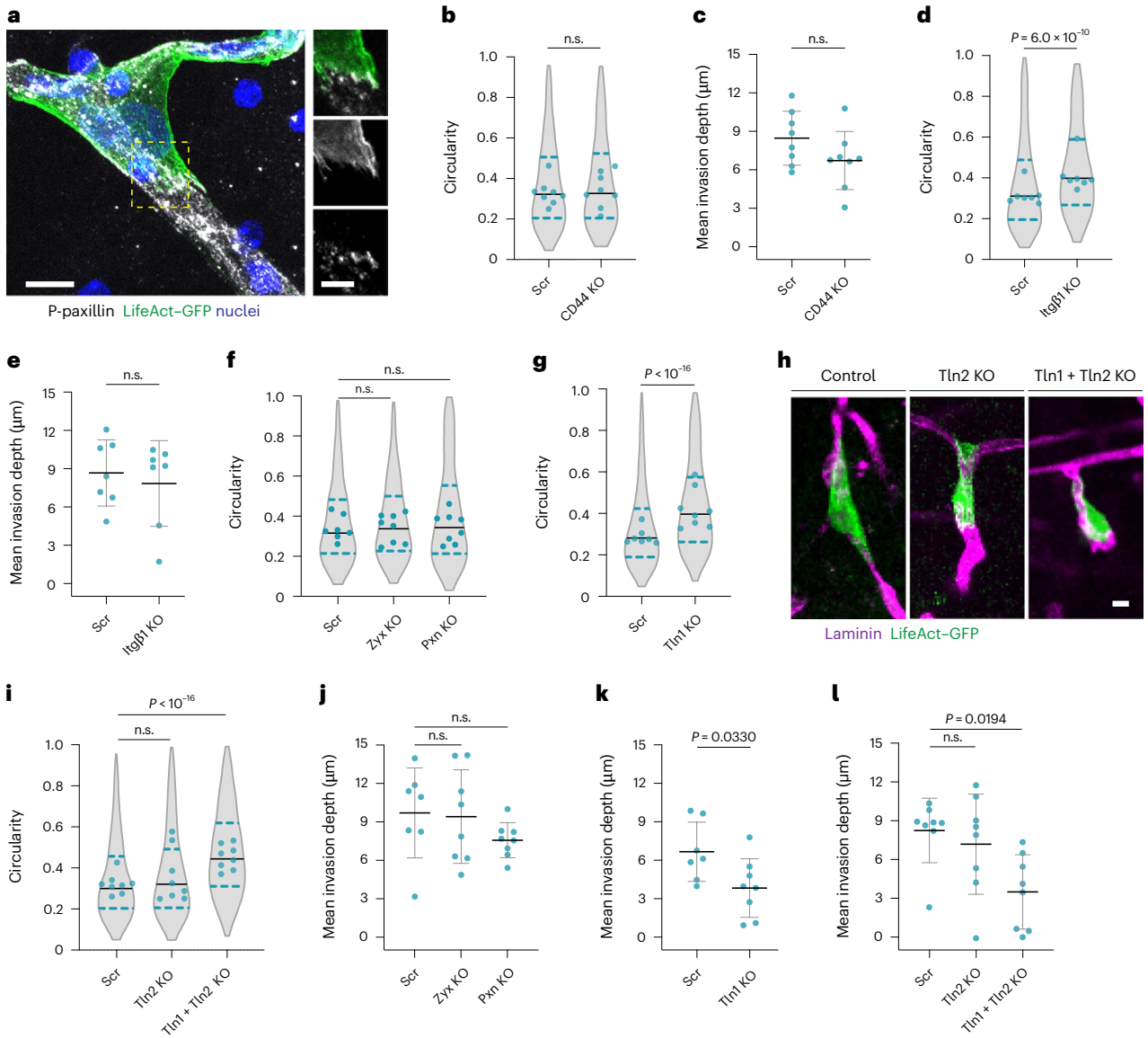

Fig. 2 | Talin-driven migration regulates vessel co-option. a, A brain slice immunostaining of paxillin (grey), LifeAct–GFP (green) and nuclei (Hoechst, blue) (maximum projection of 24- and 3-μm-thick stacks (inset)). Scale bars, 10 μm and 5 μm (inset). Yellow dashed lines label the zoomed areas. The images are representative of three experiments. **b**–**l**, KO experiments. Graphs show data for cells adhered to the vasculature. Violin plots of cell shape circularities for scramble control (Scr) and CD44-KO cells (Scr: $n = 652$ and CD44 KO: $n = 511$ for eight slices and four experiments). **c**, The mean invasion depth per slice for scramble control and CD44-KO cells ($n = 8$ for four experiments). **d**, Violin plots of cell shape circularities for scramble control and integrin β1-KO cells (Scr: $n = 720$ and Itgβ1 KO: $n = 354$ for seven slices and four experiments). **e**, The mean invasion depth per slice for scramble control and integrin β1-KO cells ($n = 7$ for four experiments). **f**, Violin plots of cell shape circularities for scramble control, zyxin-KO and paxillin-KO cells (Scr: $n = 593$ for seven slices; Zyx KO: $n = 704$ for eight slices; and Pxn KO: $n = 597$ for eight slices (four experiments)). **g**, Violin plots of cell shape circularities for scramble control and talin 1-KO cells (Scr: $n = 826$ for seven slices; Tln1 KO: $n = 725$ for eight slices (four experiments)). **h**, Immunostaining of laminin (magenta) and LifeAct–GFP (green) showing scramble control, talin 2-KO and talin 1- and talin 2-KO cells (maximum projection; scale bar, 10 μm). **i**, Violin plots of cell shape circularities for scramble control, talin 2-KO and talin 1- and talin 2-KO cells (Scr: $n = 717$, Tln2 KO: $n = 640$ and Tln1 + Tln2 KO: $n = 544$ for eight slices and four experiments). **j**, The mean invasion depth per slice for scramble control, zyxin-KO and paxillin-KO cells ($n = 7$ for Scr and $n = 8$ for Zyx KO and Pxn KO for four experiments). **k**, The mean invasion depth per slice for scramble control and talin 1-KO cells ($n = 7$ for Scr and $n = 8$ for Tln1 KO for four experiments). **l**, The mean invasion depth per slice for scramble control, talin 2-KO and talin 1- and talin 2-KO cells ($n = 8$ for four experiments). The violin plots show the median ± interquartile range, and the dots represent median values per slice. n.s., not significant. For the statistical analysis, a two-sided Mann–Whitney or a Kruskal–Wallis test followed by a post hoc Dunn's test (for **f** and **i**) was performed. The mean invasion depth graphs show the mean ± standard deviation. For the statistical analysis, a two-sided *t*-test or an ordinary one-way analysis of variance test followed by a post hoc Tukey's test (for **j** and **l**) was performed.

the phenotype of increased invasion along the vasculature compared with through the bulk (Fig. 4d).

While decellularization preserved the ECM composition of the slices, the process additionally induced substantial shrinkage of the tissue, probably modifying its structural and mechanical properties. To study the specific contribution of the basement membrane ECM to both cell spreading and migration along the vasculature in a more controlled context, we developed a microfluidic device to model vessel co-option. Within a microfluidic polydimethylsiloxane (PDMS) device, we filled a chamber with a mixture of HA and collagen type I to represent brain ECM and used a needle to generate a cylindrical lumen in the matrix (Fig. 4e)[33]. The lumen was seeded with human microvascular

https://doi.org/10.1038/s41556-024-01532-6

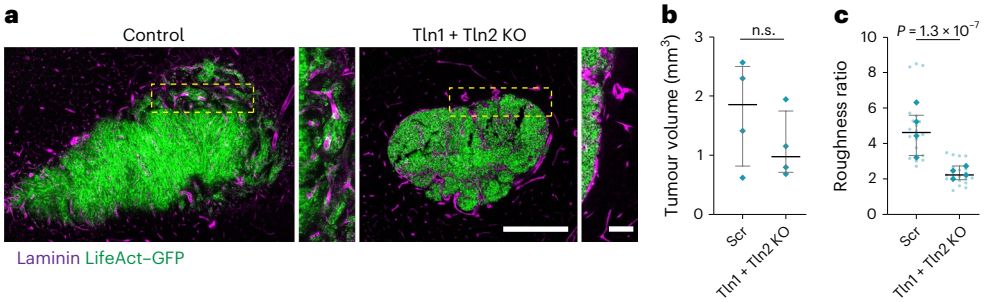

Fig. 3 | Talin-KO tumours have smoother boundaries and lose the association with the vasculature at the invasive front. a, Immunostaining of laminin (magenta) and LifeAct–GFP (green) showing scramble control (Scr) and talin 1- and talin 2-KO tumours 1 week after injection. Yellow dashed lines label zoomed areas. Scale bars, 500 µm and 10 µm (inset). **b**, Tumour volumes for scramble control and talin 1- and talin 2-KO tumours ($n = 4$ animals). The graph shows the median ± interquartile range. For the statistical analysis, a two-sided Mann–Whitney test was performed. **c**, The edge roughness ratio for scramble control and talin 1- and talin 2-KO tumours (Scr: $n = 22$ and Tln1 + Tln2 KO: $n = 21$ for four animals). n.s., not significant. The lighter dots represent single plane values and the darker dots the mean value per tumour. The graph shows the mean ± standard deviation. For the statistical analysis, a two-sided t-test was performed.

brain endothelial cells (HMBEC) to form an engineered micro-vessel, and melanoma cells were embedded in the three-dimensional (3D) bulk gel. Within 2 days, HMBECs deposited a laminin-rich ECM layer lining the channel. During that time, some of the cancer cells started to migrate along the vessel, allowing us to study vessel co-option in vitro (Fig. 4f). To validate this model to the observations made in brain slices, we analysed 3D cell shapes of melanoma cells within the bulk hydrogel or adhered to the engineered vessel. Similar to the brain slices, the sphericity of cells moving along the vessel was significantly lower than those in the bulk (Fig. 4g,h). Further, talin 1 and talin 2 double-KO cells showed increased sphericities and reduced migration velocities along the channel (Extended Data Fig. 6a–c). Together, these results suggest that the microfluidic model captured the essential aspects of vessel co-option in vitro.

To evaluate if the presence of basement membrane is critical for the elongation and migration of melanoma cells along the engineered vessel, we leveraged three different approaches. First, we coated the channel with basement membrane extract (BME) without seeding endothelial cells (Fig. 4i) and found that melanoma cells spreading along the channel were significantly rounder in the ECM coating condition compared with control endothelialized vessels (Fig. 4i,j). Second, we confined cells between the basement membrane and the bulk gel by completely filling the central channel with a BME gel to better recapitulate a fully crosslinked basement membrane ECM (Fig. 4i). The sphericity of melanoma cells again remained higher than in endothelialized devices (Fig. 4j), and the cells moving along the channel showed significantly reduced velocities (Fig. 4k). Third, to exclude the possibility of meaningful differences in composition between BME and endothelial cell-deposited ECM, we seeded endothelial cells infected with an inducible split caspase-9 (iCasp)[34] to selectively remove the endothelial cells from the vessel after they deposited a basement membrane (Fig. 4l–o). Following a 24 h period of basement membrane deposition by the iCasp endothelial cells, a small chemical inducer of dimerization (CID) was administered to induce caspase activation, rapidly triggering cell apoptosis and leaving only the layer of endothelial cell-deposited ECM in the microfluidic channel. These devices were cultured without endothelial cells for an additional 12 h before fixation and staining. Although laminin was still present 12 h after eliminating the endothelial cells, the overall signal intensity was reduced compared with control vessels (Fig. 4l,m and Extended Data Fig. 6d). To account for the effect of ECM density, we compared the sphericities of cancer cells spread on similar ECM intensity levels. Again, we observed that cells adhering the basement membrane alone were significantly rounder than those in the presence of endothelial cells (Fig. 4n,o and Extended Data Fig. 6e). Together, these results suggest that the presence of a basement membrane ECM is not sufficient to recapitulate the level of cell spreading or the migration along the vasculature observed in brain tissue.

Vascular stiffness promotes cell spreading and invasion

The brain is one of the softest organs, with a rigidity of a few hundred pascals. Focal adhesions are regulated not only by the type of ECM but also by its mechanical properties[21]. Indeed, talin not only is a scaffolding protein important for focal adhesions but also is a mechanosensor[35]. Above a certain stiffness threshold where cell–ECM adhesions are submitted to high enough forces, talin unfolds, allowing for vinculin binding to the newly exposed sites and triggering focal adhesion strengthening[36–38]. To test if vessel co-option requires talin mechanosensing, we generated a vinculin-KO cell line (second clone in Extended Data Fig. 7). Similarly to the talin 1 and talin 2 double-KO, invasion via the vasculature through brain slices was significantly reduced in the absence of vinculin (Fig. 5a and Extended Data Fig. 7).

These observations suggest that, in the brain, blood vessels could be stiffer than the surrounding tissue, thereby providing a favourable mechanical substrate for cancer cells to spread and migrate along. To test this hypothesis, we measured the relative stiffness between the microvasculature and the bulk brain tissue using atomic force microscopy (AFM). To be able to visualize and target vessels at the surface of a tissue slice, we used 20-µm-thick cryosections (Fig. 5b). Although brain cryosections were softer than fresh tissue slices (Extended Data Fig. 8a,b), measuring the stiffness of micro-vessels compared with a nearby area revealed that vessels were significantly stiffer than the tissue surrounding them (Fig. 5c,d and Extended Data Fig. 8c).

One possibility for why vessel co-option is lost when endothelial cells are removed is that endothelial cells themselves contribute to the stiffness of the vasculature. To test this possibility, we decreased endothelial cell stiffness in our in vitro model by knocking out myosin-IIa in endothelial cells (Fig. 5e and Extended Data Fig. 8d,e). Notably, the stiffness of the surrounding HA-collagen gel was below 350 Pa, comparable with bulk brain tissue (Extended Data Fig. 8f). While devices seeded with control and myosin-IIa-KO HMBECs maintained similar levels of deposited ECM (Fig. 5f,g), melanoma cells showed significantly reduced spreading along the myosin-IIa-KO micro-vessels (Fig. 5h). To explore the potential effect of vessel stiffness in brain slices, we employed a dextran methacrylate gel to fill the vasculature and stiffen the vessel network before slicing (Extended Data Fig. 8g). To accomplish this, mice were perfused with a liquid prepolymer mix of dextran methacrylate and a polyethylene glycol (PEG) crosslinker that quickly polymerized after perfusion (Fig. 5i). Animals received either isolectin with no gel to label vessels as a control or one of two different gel formulations of different stiffnesses (~3 and 100 kPa; Fig. 5j,k). When

https://doi.org/10.1038/s41556-024-01532-6

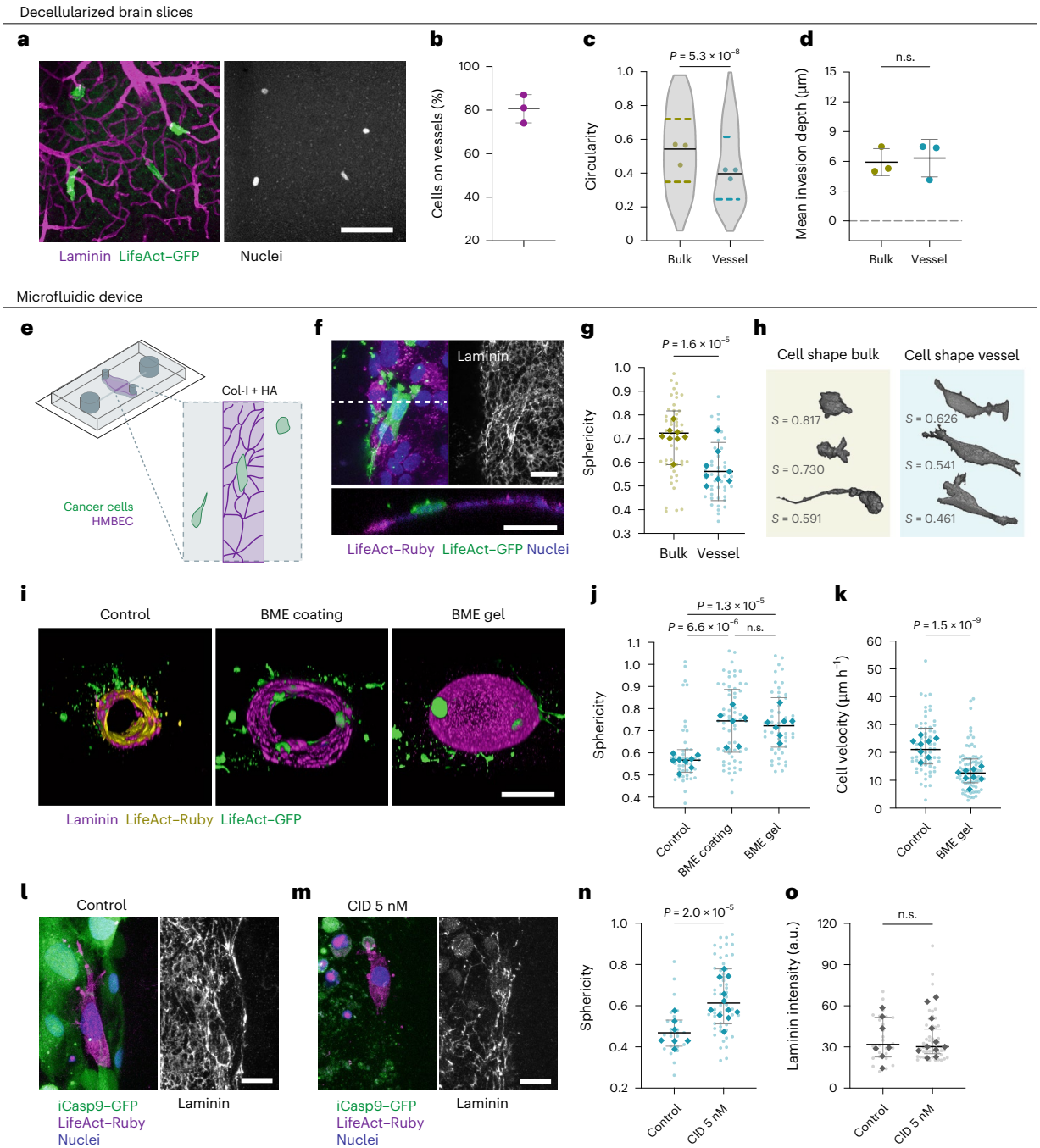

Fig. 4 | The ECM composition of the basement membrane is not sufficient to drive spreading and invasion of melanoma cells along the vasculature. **a**, Decellularized slices. Brain slice immunostaining of laminin (magenta), LifeAct–GFP (green) and nuclei (Hoechst, grey) (maximum projection; scale bar, 100 µm). **b**, The percentage of cells adhered to the basement membrane ($n = 3$ experiments). **c**, Violin plots of cell shape circularities for cells adhered to the basement membrane (vessels) or the bulk (bulk: $n = 191$, vessel: $n = 743$ for 11 slices and three experiments). The dots represent the median values per experiment. For the statistical analysis, a two-sided Mann–Whitney test was performed. The graph shows the median ± interquartile range. **d**, The mean invasion depth for cells adhered to vessels or the bulk ($n = 3$ experiments). For the statistical analysis, a two-sided paired *t*-test was performed. The graph shows the mean ± standard deviation. **e**, Microfluidic device. Schematic of the device modelling in vitro vessel co-option. **f**, Immunostaining of laminin (grey), 1205Lu LifeAct–GFP (green), HMBEC LifeAct–Ruby (magenta) and nuclei (Hoechst, blue). Top: maximum projection. Bottom: *XZ* plane along the dashed line. Scale bar, 20 µm. **g**, 1205Lu cell sphericity on the micro-vessel or in the bulk gel (bulk: $n = 47$, vessel: $n = 47$ for eight devices and three experiments). **h**, Representative 3D cell shapes from **g** (sphericities indicated, S). **i**, Immunostaining of laminin (magenta), 1205Lu LifeAct–GFP (green) and HMBEC LifeAct–Ruby (yellow) in control, BME-coating and BME-gel devices (3D views). Scale bar, 100 µm. **j**, The sphericity of cells adhered to the micro-vessel in control, BME-coating and BME-gel devices (control: $n = 46$ for eight devices; BME coating: $n = 61$ for six devices; BME gel: $n = 50$ for seven devices and three experiments). **k**, The velocity of cells along the micro-vessel in control or BME gel devices (control: $n = 83$, BME gel: $n = 65$ for eight devices and three experiments). **l**,**m**, Immunostaining of laminin (grey), 1205Lu LifeAct–Ruby (magenta), HMBEC iCasp9–GFP (green) and nuclei (Hoechst, blue) in control (**l**) and 5 nM CID (**m**) devices. Scale bar, 20 µm. **n**,**o**, The cell sphericity (**n**) and laminin intensity (**o**) of cells spreading on control or CID-induced endothelial cell apoptosis devices (control: $n = 26$ for seven devices; CID 5 nM: $n = 54$ for 11 devices (for four experiments)). Only cells with substantial laminin intensity are shown for CID. The full data are in Extended Data Fig. 6. n.s., not significant. The lighter dots and the darker dots represent individual cells and device medians. For the statistical analysis, a two-sided Mann–Whitney or a Kruskal–Wallis test followed by a post hoc Dunn's test (for **j**) was performed. The graphs show the median ± interquartile range.

https://doi.org/10.1038/s41556-024-01532-6

measuring perfused micro-vessels with AFM using cryosections, vessels perfused with the stiff formulation showed a fivefold increase in stiffness compared with vessels perfused with soft dextran (Extended Data Fig. 8h,i). Perfused brains were sliced, and melanoma cells were added for 24 h ex vivo culture as before (Extended Data Fig. 8j). Stiffening the vasculature did not further increase the degree of spreading of cancer cells along the vasculature (Fig. 5l), but cells in the stiff dextran condition invaded brain slices significantly more than in the control

Fig. 5 | The differential stiffness of the vessel network versus surrounding tissue promotes cell spreading and invasion. a, The mean invasion depth per slice for scramble control (Scr) and vinculin-KO cells adhered to the vasculature ($n = 5$ for three experiments). For the statistical analysis, a two-sided *t*-test was performed. The graph shows the mean ± standard deviation. **b**, Isolectin-IB4 staining of vasculature in a 20 µm cryosection. Scale bar, 100 µm. **c**, Left: isolectin-IB4 images showing vessel and bulk locations for AFM indentation (yellow dots). Right: corresponding force-indentation curves. The grey dashed lines show curve fittings. Scale bar, 20 µm. **d**, The Young's modulus of vessels and surrounding tissue ($n = 40$ for four brains). For the statistical analysis, a two-sided Wilcoxon test was performed. **e**, The Young's modulus of scramble control and myosin-IIa-KO HMBECs (Scr: $n = 73$, Myh9 KO: $n = 60$ for three experiments). For the statistical analysis, a two-sided Mann–Whitney test was performed. The lighter and darker dots represent each indentation and the median value per experiment. **f**, Immunostaining of HMBEC LifeAct–Ruby (grey), 1205Lu LifeAct–GFP (green) and nuclei (Hoechst, blue) in scramble control and myosin-IIa-KO micro-vessels (maximum projection; scale bar, 20 µm). **g**,**h**, The laminin intensity (**g**) and cell sphericity (**h**) for cells spreading on scramble control or myosin-IIA-KO devices (control: $n = 68$ for ten devices; Myh9 KO: $n = 70$ for 14 devices (three experiments)). For the statistical analysis, a two-sided Mann–Whitney test was performed. The lighter and darker dots represent each cell value and device medians. **i**, A schematic of the dextran perfusion experiment. The brain slice image shows labelled dextran gel. Scale bar, 100 µm. **j**, The mean Young's modulus for each perfused dextran gel ($n = 3$ experiments). The graph shows the mean ± standard error of the mean. **k**, A brain slice immunostaining of laminin (blue, inset), isolectin or dextran (magenta) and LifeAct–GFP (green) for brains perfused with isolectin-IB4, a soft or a stiff dextran gel (maximum projection; scale bars, 100 µm and 20 µm (inset)). **l**, Violin plots of cell shape circularities for cells adhered to the vasculature on control, soft or stiff dextran (control: $n = 1{,}349$ for 11 slices; soft: $n = 1{,}278$ for 11 slices; stiff: $n = 1{,}050$ for 10 slices (3 experiments)). The dots represent the median circularity per slice. For the statistical analysis, a Kruskal–Wallis test, followed by a post hoc Dunn's test, was performed. **m**, The mean invasion depth per slice for cells adhered to the vasculature on control, soft or stiff dextran (control: $n = 11$, soft: $n = 11$, stiff: $n = 10$ for three experiments). For the statistical analysis, an ordinary one-way analysis of variance test, followed by a post hoc Tukey's test, was performed. The graph shows the mean ± standard deviation. **n**, A schematic of the double-layer gel assay; orthogonal view: fluorescent beads (blue, top gel; magenta, bottom gel) and LifeAct–GFP (green). Scale bar, 20 µm. **o**, The mean Young's modulus of each gel condition ($n = 3$ experiments). The graph shows mean ± standard error of the mean. **p**, Violin plots of cell velocities for cells migrating between gels (soft–soft: $n = 163$, soft–stiff: $n = 211$, stiff–stiff: $n = 177$ for three experiments). n.s., not significant. The dots represent the median cell velocity for each experiment. For the statistical analysis, a Kruskal–Wallis test, followed by a post hoc Dunn's test, was performed. The figure graphs show the median ± interquartile range unless stated otherwise. The drawings in **c** and **i** were created with BioRender.com.

or soft gel conditions (Fig. 5m and Extended Data Fig. 8k,l). These results demonstrate that melanoma cells respond to the stiffness of the vasculature, whereby a stiffer vascular network stimulates faster invasion into brain tissue.

One remaining question was whether migration along vessels was determined only by vascular stiffness or also by the contrasting softness of the surrounding tissue parenchyma. To test this, we developed a double-layered gel assay (Fig. 5n). Melanoma cells were seeded on an alginate gel containing BME (modelling vasculature) and covered with a second non-adhesive alginate gel (modelling brain tissue). When both gels were soft with a Young's modulus mimicking brain stiffness (Fig. 5o), cells at the interface between the two gels exhibited rounded shapes and negligible velocities (Fig. 5p). When exposed to a stiffer bottom gel and a soft top gel (Fig. 5o), cell velocities significantly increased mimicking vessel co-option (Fig. 5p). Remarkably, although adhesion to a stiffer substrate enhanced migration, when combined with a stiff top gel, migration was significantly reduced (Fig. 5p and Extended Data Fig. 8m,n). Together, these observations suggest that the differential stiffness between the vasculature and the brain parenchyma promotes vessel co-option.

Discussion

The role of the vasculature in cancer progression has long been investigated. To grow, tumours need access to the oxygen and nutrients delivered by vessels. To gain such access, they can both trigger an angiogenic response to induce the formation of new blood vessels[39–41] or hijack the existing vasculature[42]. However, the role of vasculature as migratory paths for cancer cells to invade through tissues is largely unexplored. Thanks to intravital microscopy, this phenomenon has been described and visualized in the brain in cells from both gliomas or metastases from breast, lung and skin cancer; although, quantitative characterization of the process has been challenging[16,17,43–45]. Here, using brain slices as an alternative approach, we show that not only metastatic cancer cells but also many adherent cell types preferentially migrate along the vasculature in the brain, suggesting that the machinery for vessel co-option is relatively common if not universal in adherent cells.

Specific interactions between adhesion receptors and the brain vasculature have been shown to contribute to vessel co-option. Cancer cells can directly interact with brain endothelial cells through the adhesion molecule L1CAM[11,18] or the family of GAP junction proteins connexins[46]; although, it is unclear if that interaction is initiated on the apical rather than basolateral interface of the endothelium. Additionally, cancer cells can adhere to the basement membrane ECM via integrins[10,14,28]. Carbonell et al. showed that blocking integrin β1 significantly reduced adhesion of metastatic cells to vessels[10]. In our model, integrin β1-KO cells also exhibited a lower degree of spreading on vasculature; although, the extent of invasion into the brain tissue was unaffected, probably due to integrin subtype redundancy. Consistent with these findings, inhibition of integrins has not shown a significant clinical success in preventing cancer progression[29,47]. Upstream of integrins, adaptor proteins provide an alternative target for blocking cancer migration. During metastasis, inhibiting talin in circulating tumour cells hinders extravasation, significantly reducing the number of metastases formed[48–50]. In this study, we find that inhibiting talin also significantly reduces metastatic cell spreading and migration along the brain vasculature.

The role of talin in rigidity sensing led us to hypothesize that vascular stiffness, in addition to ECM composition, plays a critical role in vessel co-option (Extended Data Fig. 9). While brain stiffness had been measured previously[51], we report a stiffness differential between the microvasculature and the surrounding tissue. Previous work has shown that stiffening the vascular basement membrane enhances the transmigration of circulating metastatic cells, increasing the number of metastatic sites[52]. Here, in the context of vessel co-option, we found that increasing stiffness of the vasculature caused melanoma cells to increase their speed of invasion along vessels. This is consistent with studies of adhesion-dependent migration on flat surfaces, where stiff substrates can promote more efficient migration[36,53]. An open question arising from our work is whether changes in brain vasculature stiffness, for example, from aging or hypertension, could enhance vessel co-option and cancer invasiveness. The role of blood flow has been studied in the context of extravasation[54,55], but how changes in blood pressure may regulate vessel co-option in the brain and other organs remains unexplored. Despite the prevalence of brain metastasis, it remains a clinical challenge with limited treatment options. Our findings highlight the potential of targeting talin or other components of the rigidity mechanosensing pathway in metastatic cells to attenuate vessel co-option. Beyond migration, adhesion and spreading along the vasculature has been linked to the regulation of metastatic cell survival, proliferation and dormancy[11,16,43]. Future studies are needed to explore the role of the vascular mechanical properties in these processes.

Our studies suggest that vascular stiffness and surrounding tissue softness work together to influence invasion. One explanation is that the surrounding matrix may confine cells, preventing their movement along the interface. Unlike durotaxis, where cells follow gradients of stiffness[56], we describe a distinct mode of migration where cells move at the interface between regions of different stiffnesses. By embedding cells between alginate gels, we confirmed that although adhesion to a stiffer substrate enhances migration, confinement by a secondary stiff gel greatly reduces motility. Supporting this notion is work showing that 3D nano-porous stiff environments, which still promote focal adhesion formation, are much harder to deform and migrate through and can confine cells by restricting their migration[57–59]. Regardless, these findings highlight the importance of appreciating the inherently heterogeneous nature of native tissue microenvironments, in both composition and mechanical properties, and that cells have evolved numerous mechanisms to sense and navigate through that complexity. Developing different approaches to model and perturb these spatially heterogeneous tissue microenvironments will be critical to deepening our understanding of how cancers disseminate through our bodies.

Online content

Any methods, additional references, Nature Portfolio reporting summaries, source data, extended data, supplementary information, acknowledgements, peer review information; details of author contributions and competing interests; and statements of data and code availability are available at https://doi.org/10.1038/s41556-024-01532-6.

References

1. Paul, C. D., Mistriotis, P. & Konstantopoulos, K. Cancer cell motility: lessons from migration in confined spaces. *Nat. Rev. Cancer* **17**, 131–140 (2017).
2. Riching, K. M. et al. 3D collagen alignment limits protrusions to enhance breast cancer cell persistence. *Biophys. J.* **107**, 2546–2558 (2014).
3. Fraley, S. I. et al. Three-dimensional matrix fiber alignment modulates cell migration and MT1-MMP utility by spatially and temporally directing protrusions. *Sci. Rep.* **5**, 14580 (2015).
4. Provenzano, P. P. et al. Collagen reorganization at the tumor-stromal interface facilitates local invasion. *BMC Med* **4**, 38 (2006).
5. Alexander, S., Koehl, G. E., Hirschberg, M., Geissler, E. K. & Friedl, P. Dynamic imaging of cancer growth and invasion: a modified skin-fold chamber model. *Histochem. Cell Biol.* **130**, 1147–1154 (2008).
6. Marcadis, A. R. et al. Rapid cancer cell perineural invasion utilizes amoeboid migration. *Proc. Natl Acad. Sci. USA* **120**, e2210735120 (2023).
7. Weigelin, B., Bakker, G.-J. & Friedl, P. Intravital third harmonic generation microscopy of collective melanoma cell invasion. *Intravital* **1**, 32–43 (2012).
8. Beunk, L., Brown, K., Nagtegaal, I., Friedl, P. & Wolf, K. Cancer invasion into musculature: mechanics, molecules and implications. *Semin. Cell Dev. Biol.* **93**, 36–45 (2019).
9. Bentolila, L. A. et al. Imaging of angiotropism/vascular co-option in a murine model of brain melanoma: implications for melanoma progression along extravascular pathways. *Sci. Rep.* **6**, 23834 (2016).
10. Carbonell, W. S., Ansorge, O., Sibson, N. & Muschel, R. The vascular basement membrane as 'soil' in brain metastasis. *PLoS ONE* **4**, e5857 (2009).
11. Er, E. E. et al. Pericyte-like spreading by disseminated cancer cells activates YAP and MRTF for metastatic colonization. *Nat. Cell Biol.* **20**, 966–978 (2018).
12. Farin, A. et al. Transplanted glioma cells migrate and proliferate on host brain vasculature: a dynamic analysis. *Glia* **53**, 799–808 (2006).
13. Fornabaio, G. et al. Angiotropism and extravascular migratory metastasis in cutaneous and uveal melanoma progression in a zebrafish model. *Sci. Rep.* **8**, 10448 (2018).
14. Gritsenko, P. G. & Friedl, P. Adaptive adhesion systems mediate glioma cell invasion in complex environments. *J. Cell Sci.* **131**, jcs216382 (2018).
15. Hirata, E. et al. In vivo fluorescence resonance energy transfer imaging reveals differential activation of Rho-family GTPases in glioblastoma cell invasion. *J. Cell Sci.* **125**, 858–868 (2012).
16. Kienast, Y. et al. Real-time imaging reveals the single steps of brain metastasis formation. *Nat. Med.* **16**, 116–122 (2010).
17. Winkler, F. et al. Imaging glioma cell invasion in vivo reveals mechanisms of dissemination and peritumoral angiogenesis. *Glia* **57**, 1306–1315 (2009).
18. Valiente, M. et al. Serpins promote cancer cell survival and vascular co-option in brain metastasis. *Cell* **156**, 1002–1016 (2014).
19. Charras, G. & Sahai, E. Physical influences of the extracellular environment on cell migration. *Nat. Rev. Mol. Cell Biol.* **15**, 813–824 (2014).
20. Mekhdjian, A. H. et al. Integrin-mediated traction force enhances paxillin molecular associations and adhesion dynamics that increase the invasiveness of tumor cells into a three-dimensional extracellular matrix. *Mol. Biol. Cell* **28**, 1467–1488 (2017).
21. Kechagia, J. Z., Ivaska, J. & Roca-Cusachs, P. Integrins as biomechanical sensors of the microenvironment. *Nat. Rev. Mol. Cell Biol.* **20**, 457–473 (2019).
22. Zimmermann, D. R. & Dours-Zimmermann, M. T. Extracellular matrix of the central nervous system: from neglect to challenge. *Histochem. Cell Biol.* **130**, 635–653 (2008).
23. Barnes, J. M., Przybyla, L. & Weaver, V. M. Tissue mechanics regulate brain development, homeostasis and disease. *J. Cell Sci.* **130**, 71–82 (2017).
24. Kim, Y. & Kumar, S. CD44-mediated adhesion to hyaluronic acid contributes to mechanosensing and invasive motility. *Mol. Cancer Res.* **12**, 1416–1429 (2014).
25. Mooney, K. L. et al. The role of CD44 in glioblastoma multiforme. *J. Clin. Neurosci.* **34**, 1–5 (2016).
26. Safarians, G. et al. Glioblastoma spheroid invasion through soft, brain-like matrices depends on hyaluronic acid–CD44 interactions. *Adv. Health. Mater.* **12**, 2203143 (2023).
27. Wolf, K. J. et al. A mode of cell adhesion and migration facilitated by CD44-dependent microtentacles. *Proc. Natl Acad. Sci. USA* https://doi.org/10.1073/pnas.1914294117 (2020).
28. Anderson, S. M., Kelly, M. & Odde, D. J. Glioblastoma cells use an integrin- and CD44-mediated motor-clutch mode of migration in brain tissue. *Cell. Mol. Bioeng.* **17**, 121–135 (2024).
29. Bergonzini, C., Kroese, K., Zweemer, A. J. M. & Danen, E. H. J. Targeting integrins for cancer therapy—disappointments and opportunities. *Front. Cell Dev. Biol.* **10**, 863850 (2022).
30. Raab-Westphal, S., Marshall, J. F. & Goodman, S. L. Integrins as therapeutic targets: successes and cancers. *Cancers* **9**, 110 (2017).
31. Haeger, A. et al. Collective cancer invasion forms an integrin-dependent radioresistant niche. *J. Exp. Med.* **217**, e20181184 (2019).
32. Bui, T. et al. Functional redundancy between β1 and β3 integrin in activating the IR/Akt/mTORC1 signaling axis to promote ErbB2-driven breast cancer. *Cell Rep.* **29**, 589–602.e6 (2019).
33. Polacheck, W. J., Kutys, M. L., Tefft, J. B. & Chen, C. S. Microfabricated blood vessels for modeling the vascular transport barrier. *Nat. Protoc.* **14**, 1425–1454 (2019).
34. Di Stasi, A. et al. Inducible apoptosis as a safety switch for adoptive cell therapy. *N. Engl. J. Med.* **365**, 1673–1683 (2011).
35. Goult, B. T., Yan, J. & Schwartz, M. A. Talin as a mechanosensitive signaling hub. *J. Cell Biol.* **217**, 3776–3784 (2018).

36. Elosegui-Artola, A. et al. Mechanical regulation of a molecular clutch defines force transmission and transduction in response to matrix rigidity. *Nat. Cell Biol.* **18**, 540–548 (2016).
37. Isomursu, A. et al. Directed cell migration towards softer environments. *Nat. Mater.* **21**, 1081–1090 (2022).
38. Austen, K. et al. Extracellular rigidity sensing by talin isoform-specific mechanical linkages. *Nat. Cell Biol.* **17**, 1597–1606 (2015).
39. Folkman, J. Tumor angiogenesis: therapeutic implications. *N. Engl. J. Med.* **285**, 1182–1186 (1971).
40. Hanahan, D. & Weinberg, R. A. Hallmarks of cancer: the next generation. *Cell* **144**, 646–674 (2011).
41. Weis, S. M. & Cheresh, D. A. Tumor angiogenesis: molecular pathways and therapeutic targets. *Nat. Med.* **17**, 1359–1370 (2011).
42. Kuczynski, E. A., Vermeulen, P. B., Pezzella, F., Kerbel, R. S. & Reynolds, A. R. Vessel co-option in cancer. *Nat. Rev. Clin. Oncol.* **16**, 469–493 (2019).
43. Dai, J. et al. Astrocytic laminin-211 drives disseminated breast tumor cell dormancy in brain. *Nat. Cancer* **3**, 25–42 (2022).
44. Griveau, A. et al. A glial signature and Wnt7 signaling regulate glioma-vascular interactions and tumor microenvironment. *Cancer Cell* **33**, 874–889.e7 (2018).
45. Voutouri, C. et al. Experimental and computational analyses reveal dynamics of tumor vessel cooption and optimal treatment strategies. *Proc. Natl Acad. Sci. USA* **116**, 2662–2671 (2019).
46. Stoletov, K. et al. Role of connexins in metastatic breast cancer and melanoma brain colonization. *J. Cell Sci.* **126**, 904–913 (2013).
47. Slack, R. J., Macdonald, S. J. F., Roper, J. A., Jenkins, R. G. & Hatley, R. J. D. Emerging therapeutic opportunities for integrin inhibitors. *Nat. Rev. Drug Discov.* **21**, 60–78 (2022).
48. Barbazán, J. et al. Liver metastasis is facilitated by the adherence of circulating tumor cells to vascular fibronectin deposits. *Cancer Res.* **77**, 3431–3441 (2017).
49. Beaty, B. T. et al. Talin regulates moesin–NHE-1 recruitment to invadopodia and promotes mammary tumor metastasis. *J. Cell Biol.* **205**, 737–751 (2014).
50. Sakamoto, S., McCann, R. O., Dhir, R. & Kyprianou, N. Talin1 promotes tumor invasion and metastasis via focal adhesion signaling and anoikis resistance. *Cancer Res.* **70**, 1885–1895 (2010).
51. Budday, S., Ovaert, T. C., Holzapfel, G. A., Steinmann, P. & Kuhl, E. Fifty shades of brain: a review on the mechanical testing and modeling of brain tissue. *Arch. Comput. Methods Eng.* **27**, 1187–1230 (2020).
52. Reuten, R. et al. Basement membrane stiffness determines metastases formation. *Nat. Mater.* **20**, 892–903 (2021).
53. Bangasser, B. L. et al. Shifting the optimal stiffness for cell migration. *Nat. Commun.* **8**, 15313 (2017).
54. Osmani, N. et al. Metastatic tumor cells exploit their adhesion repertoire to counteract shear forces during intravascular arrest. *Cell Rep.* **28**, 2491–2500.e5 (2019).
55. Follain, G. et al. Hemodynamic forces tune the arrest, adhesion, and extravasation of circulating tumor cells. *Dev. Cell* **45**, 33–52. e12 (2018).
56. Shellard, A. & Mayor, R. Durotaxis: the hard path from in vitro to in vivo. *Dev. Cell* **56**, 227–239 (2021).
57. Chang, J., Pang, E. M., Adebowale, K., Wisdom, K. M. & Chaudhuri, O. Increased stiffness inhibits invadopodia formation and cell migration in 3D. *Biophys. J.* **119**, 726–736 (2020).
58. Wang, C., Tong, X. & Yang, F. Bioengineered 3D brain tumor model to elucidate the effects of matrix stiffness on glioblastoma cell behavior using PEG-based hydrogels. *Mol. Pharm.* **11**, 2115–2125 (2014).
59. Singh, S. P., Schwartz, M. P., Lee, J. Y., Fairbanks, B. D. & Anseth, K. S. A peptide functionalized poly (ethylene glycol) (PEG) hydrogel for investigating the influence of biochemical and biophysical matrix properties on tumor cell migration. *Biomater. Sci.* **2**, 1024–1034 (2014).

[1]Department of Biomedical Engineering, Boston University, Boston, MA, USA. [2]The Wyss Institute for Biologically Inspired Engineering, Harvard University, Boston, MA, USA. [3]Biological Design Center, Boston University, Boston, MA, USA. [4]Harvard–MIT Program in Health Sciences and Technology, Institute for Medical Engineering and Science, Massachusetts Institute of Technology, Cambridge, MA, USA. [5]Cell and Tissue Mechanobiology Laboratory, The Francis Crick Institute, London, UK. [6]Department of Physics, King's College London, London, UK. [7]Department of Surgery, University of California, San Francisco, CA, USA. [8]Center for Bioengineering and Tissue Regeneration, University of California San Francisco, San Francisco, CA, USA. [9]Department of Chemical Engineering, University of New Hampshire, Durham, NH, USA. [10]UCSF Helen Diller Comprehensive Cancer Center, University of California San Francisco, San Francisco, CA, USA. [11]Department of Radiation Oncology, Eli and Edythe Broad Center of Regeneration Medicine and Stem Cell Research, University of California San Francisco, San Francisco, CA, USA. ✉e-mail: chencs@bu.edu

Methods

The research in this work complies with all of the relevant ethical regulations. All animal studies were approved and performed in accordance with guidelines of Boston University' Institutional Animal Care and Use Committees (protocol no. 201800528). Human blood collection was performed under a protocol (no. 18-1537) approved by the Institutional Review Board at Boston University. All human donors provided informed consent, were not compensated and their demographic information (sex, age and so on) were not recorded.

Cell culture

The 1205Lu, WM983B, U2OS, MCF7 (HTB-22, ATCC), MDA-MB-231 (HTB-26, ATCC), MDA-MB-231 TGL, MDA-231-BoM-1833, MDA-231-BrM2-831, MDA-231-LM2-4175, A375P (CRL-3224, ATCC), A375M2 (CRL-3223, ATCC), B16-F10 and EO771 cancer cell lines; NIH-3T3 mouse fibroblasts (CRL-1658, ATCC); and HEK-293T cells (632180, Clontech) were cultured in Dulbecco's modified Eagle medium (10-013-CV, Corning), supplemented with 10% foetal bovine serum (SH30084.03, Hyclone) and 1% penicillin–streptomycin (15140122, Gibco). 1205Lu, WM983B and B16-F10 cell lines were a gift from R.M. Alani, EO771 were a gift from H.T. Nia, U2OS cells were a gift from C.M. Waterman and the MDA cell lines developed by J. Massagué were obtained through the Antibody and Bioresource Core Facility at MSKCC. nHDF (CC-2509, Lonza) were cultured in fibroblast growth medium-2 (CC-3132, Lonza) before passage 5 (p5) and in cancer cell medium between p5 and p10. MCF10A cells (CRL-10317, ATCC) were cultured in Dulbecco's modified Eagle medium/F12 (11330057, Gibco) supplemented with 5% horse serum (16050122, Gibco), 20 ng ml^{-1} human epidermal growth factor (AF-100-15, Peprotech), 0.5 mg ml^{-1} hydrocortisone (H0888, Sigma), 100 ng ml^{-1} cholera toxin (C8052, Sigma), 10 µg ml^{-1} insulin (I1882, Sigma) and 1% penicillin–streptomycin[60]. HBVPC (1200, ScienCell) were cultured in pericyte medium (1201, ScienCell) before p5 and in cancer cell medium between p5 and p9. Primary peripheral blood mononuclear cells were obtained from whole peripheral blood from healthy donors. Primary peripheral blood mononuclear cells were isolated using Lymphoprep (NC0418243, StemCellTechnologies), and CD3$^+$ T cells were enriched using RosetteSep Human T Cell Enrichment Cocktail (15021, StemCellTechnologies). CD3$^+$ T cells were activated using Immunocult Human CD3/CD28 T Cell Activator (10971, StemCellTechnologies) with 200 U ml^{-1} IL-2 media. Upon culturing, primary T cells were cultured in X-Vivo 15 medium (04418Q, Lonza) supplemented with 5% human AB serum (HP1022, Valley Biomedical), 10 mM *N*-acetyl L-cysteine (A9165, Sigma), 55 mM 2-mercaptoethanol (21985023, ThermoFisher) and 50–200 U ml^{-1} IL-2 (NCI BRB Preclinical Repository). The cells were used for experiments between 1 and 2 weeks after thawing. Primary HMBECs (ACBRI 376, CellSystems) were cultured in microvascular endothelial cell growth medium (EGM2-MV, CC-3202, Lonza) and used before p9. All cells were cultured at 37 °C and 5% CO_2 in a humidified incubator.

Brain slice culture

Brains from 7- to 17-week-old male and female FVB/NJ mice (001800, Jackson Laboratory) were dissected in a chilled and oxygenated N-methyl-D-glucamine (NMDG)-based solution, embedded in 2% agarose (BP1356, Fisher) and cut into eight 300 µm slices using a vibratome (Leica VT 1200; v = 0.14 mm s^{-1}, amplitude of 1 mm). To prepare the NMDG-based slicing solution[61], a solution of 93 mM NMDG (M2004, Sigma), 2.5 mM KCl (3040-01, JB Baker), 1.2 mM NaH_2PO_4 (3818-01, JB Baker), 30 mM $NaHCO_3$ (S6014, Sigma), 20 mM HEPES buffer (H7006, Sigma), 25 mM d-glucose (G8270, Sigma), 5 mM ascorbate (A7631, Sigma), 3 mM pyruvate (P5280, Sigma), 10 mM $MgCl_2$ (2444-01, JT Baker), 0.5 mM $CaCl_2$ (C-7902, Sigma), 93 mM HCl (1090571003, Sigma) and 1 mM kynurenic acid (K3375, Sigma) was prepared. $MgCl_2$, $CaCl_2$ and kynurenic acid were added last after adjusting pH with HCl to 7.3–7.4, and the solution was sonicated for 5 min to dissolve the kynurenic acid. The solution was prepared 1–2 days before slicing, kept at 4 °C and bubbled for 20 min before slicing. After slicing, slices were placed on a transwell (353090, Corning) (two slices per well) in warm neuronal medium (BrainPhys, 5792, StemCell) supplemented with 1% penicillin–streptomycin. After 15 min, the medium in the upper compartment was replaced with 1 ml of medium containing 150,000–300,000 cells. If required, 10 µl of isolectin GS-IB4 (1 mg ml^{-1}, I21412, ThermoFisher) were added to the medium to fluorescently label endothelial cells. Following a 2–4 h incubation, the medium in the upper compartment was removed (leaving the medium only in the lower compartment). The slices were maintained at 37 °C and 5% CO_2 in a humidified incubator for 24 h (unless stated otherwise). For MCF10A cells, a mix of 75% brain medium and 25% MCF10A culture medium was used for the culture of brain slices.

Brain slice immunostaining

Brain slices were rinsed once with PBS and fixed in 4% paraformaldehyde (PFA; 15710, EMS) in PBS containing 1 mM $CaCl_2$ and 0.5 mM $MgCl_2$ (PBS+) for 2 h at room temperature (optimal for phospho-paxillin (p-paxillin) staining) or overnight at 4 °C. PFA was added on the upper compartment and plates were placed on a rocker. Slices were blocked with 10% donkey serum (D9663, Sigma) and 0.5% Triton X-100 (T8787, Sigma) in PBS+ for 1 h. Primary and secondary antibodies were each applied overnight at 4 °C in 10% donkey serum and 0.5% Triton X-100 in PBS+. The slices were rinsed five times over 30 min with 0.5% Triton X-100 in PBS+ between each treatment and after secondary antibody incubation (for p-paxillin staining, the slices were washed overnight at 4 °C after secondary antibody incubation). For all washes, the slices were placed on a rocker. During post-secondary washes, if required, the slices were incubated with a 1:5,000 Hoechst (H1399, ThermoFisher) solution in 0.5% Triton X-100 in PBS+ for 25 min. The slices were mounted between thin slides and square coverslips in Prolong (P36934, ThermoFisher). Mounted slices were imaged on an upright Leica TCS SP8 confocal microscope, using the LasX software. For each slice, a region of approximately 3.8 mm × 3.8 mm and 70 µm depth was imaged and analysed.

Brain slice time-lapse microscopy

The cells were seeded on slices by adding to each well 1 ml of medium containing 400,000 cells and 10 µl of isolectin GS-IB4 (1 mg ml^{-1}, I32450, ThermoFisher) to fluorescently label endothelial cells. Following a 3 h incubation, the slices were washed once with PBS to remove unattached cells and transferred upside down to a smaller transwell (one slice per well; 353180, Corning) adhered to a glass-bottom six-well plate (P06G-0-20-F, MatTek) on both lateral sides, using two layers of double coated tape (to achieve a 360 µm height; 9495LE, 3M). The medium in the upper compartment was removed and 300 µl of media containing 3 µl of Oxyfluor (OF-0005, Oxyrase) were added underneath each transwell. The time-lapse acquisitions were performed on a Dragonfly spinning-disk microscope (Andor) equipped with thermal and CO_2 control, using the Fusion software.

Cell circularity and invasion depth analysis

Cancer cell circularity and cell invasion depths within the slice were calculated using a custom-made MATLAB software. Between 60 and 200 single cells were analysed per slice, avoiding cells overlapping with each other in z. From the image stack maximum projection, single cancer cells on the slice were identified and their xy position recorded. The cell shapes were binarized by defining a proper threshold and the properties of the projected shape (including cell circularity) were computed. As a first step to compute cancer cell depths within brain slices, laminin intensity was averaged for each z position, using both the cancer cell shape (local vasculature density) and in a region approximately 150 times bigger than the cell (region vasculature density, see Extended Data Fig. 1d). Regional vascular intensity showed a peak at the top of the slice and, because of the opacity of brain tissue, decayed when going deeper into the slice. This peak was used as a reference for

cell depth measurements: 0 µm cell depth was defined as 6 µm above the peak laminin intensity. For each cell, the two-dimensional-projected shape was also used to average the LifeAct–GFP (green fluorescent protein) fluorescence intensity for each z position, and the cell depths were computed as: $\text{cell}_{\text{depth}} = z_{\max \text{GFP}} - (z_{\max \text{r.laminin}} - 6\ \mu\text{m})$. In addition, local laminin intensity was used to determine whether the cell was adhered to a vessel or in the bulk tissue. If a peak of local laminin was detected within 8 µm in z from the GFP peak, the cancer cell was categorized as adhered to a vessel.

Brain slice decellularization

Brain slices were decellularized using a protocol adapted from a previous publication[62]. Brains were cut (as described in 'Brain slice culture') into four 700 µm slices. The slices were then transferred to a transwell and subjected to three cycles of 2 h in a 4% sodium deoxycholate (D6750, Sigma) solution, a 10 min washing step in PBS supplemented with 1% penicillin–streptomycin, a 1 h incubation with a 3% Triton X-100 solution in PBS+ and a final 10 min washing step in PBS supplemented with 1% penicillin–streptomycin. To complete the three cycles, incubations took approximately 10 h. Afterwards, the slices were incubated overnight in 0.02 mg ml^{-1} DNase I (10104159001, Roche) in PBS supplemented with 1% penicillin–streptomycin. The following day, the slices were washed five times in PBS supplemented with 1% penicillin–streptomycin (adding PBS in the upper and lower compartments of the transwell) and cultured overnight in brain medium (with medium in the upper and lower compartments). For all decellularization steps described, the slices were placed on an incubated rocker at 37 °C. For each decellularized slice, the medium in the upper compartment was replaced with 1 ml of medium containing 40,000 cells, and the cells were cultured for 24 h. Finally, the slices were stained as described in 'Brain slice immunostaining'.

Lentiviral transduction and CRISPR-KO lines

Labelled cell lines were generated using either pLenti.PGK.LifeAct-Ruby.W (Rusty Lansford, Addgene plasmid no. 51009) or pLenti.PGK.LifeAct-GFP.W (Rusty Lansford, Addgene plasmid no. 51010), except for T cells that were labelled with CellTracker (C7025, Invitrogen). iCasp9–GFP HMBECs were generated using pMSCV-F-del Casp9.IRES.GFP (David Spencer, Addgene plasmid no. 15567, cloned in house to a lentivirus plasmid backbone). After infection, the GFP^+/$Ruby^+$ population (top 30%) was selected via flow-assisted cytometry (FACSMelody, BD).

CRISPR-KO 1205Lu lines were generated using the lentiCRISPRv2 system (Feng Zhang, Addgene plasmid no. 52961) or lentiCRISPRv2 neo (for talin 2 in the double KO, Brett Stringer Addgene plasmid no. 98292). The guides were cloned into the lentiCRISPRv2 plasmid at the BsmbI site, except for the CD44 lentiCRISPRv2 plasmid that was purchased (Genscript). The guides used for CRISPR are listed in Supplementary Table 1. Guides for talin 1 and talin 2 were previously published[63]. KO efficiency was verified though western blot. To increase the efficiency of the KO, talin 1, vinculin and zyxin CRISPR lines were sorted as single cells (FACSMelody, BD), and KO clonal cell lines were established and verified through western blot.

Lentivirus was produced by co-transfecting HEK-293T cells with each individual lentiviral plasmid and with the pVSVG (Bob Weinberg, Addgene plasmid no. 8454), pRSV-REV (Didier Trono, Addgene plasmid no. 12253) and pMDLg (Didier Trono, Addgene plasmid no. 12251) packaging plasmids using a calcium phosphate transfection method. The virus-containing supernatant was collected 48 h after transfection, concentrated using PEG-it Virus Precipitation Solution (LV825A-1, SBI), resuspended in PBS and flash frozen at −80 °C.

Cell lysis and western blot

The cells were lysed using lysis buffer (a 50 mM Tris–HCl (Tris, T6066, Sigma) pH 7.6, 150 mM NaCl (BP358-1, Fisher), 1% Triton X-100, 0.25% SDS buffer (4095-02, JT Baker) and 0.5% sodium deoxycholate solution) with 2× protease and phosphatase inhibitors (78442, ThermoFisher). The sample was homogenized with a 22-gauge needle (305155, BD) and spun at 15,000g for 15 min at 4 °C. The protein content was quantified using the Pierce BCA protein assay kit (23225, ThermoFisher). The supernatant was then diluted with LDS loading buffer (NP0007, ThermoFisher), and 2-mercaptoethanol (M7522, Sigma) was added to a final 5% concentration. The samples were boiled at 100 °C for 5 min and were frozen at −20 °C until needed.

For western blots, protein loading was normalized by protein content across wells. NuPAGE Bis-Tris gels (NP0322BOX, ThermoFisher) were run at 190 mV in MOPS (3-(N-morpholino)propanesulfonic acid) buffer (NP0001, ThermoFisher), and they were blotted onto a polyvinylidene difluoride membrane (88520, ThermoFisher) in a NuPAGE transfer buffer (NP00061, ThermoFisher) 1× with 10% methanol (A452-4, Fisher) at 250 mA for 90 min. The blots were blocked in Tris-buffered saline (TBST; T5912, Sigma) with 0.1% Tween (BP337, Fisher) and 5% milk (M0841, LabScientific) for 1 h. The primary antibodies were added in TBST with 5% milk overnight at 4 °C. After washing three times with TBST at room temperature, the secondary antibodies were added in TBST with 5% milk for 2 h at room temperature. After washing three times with TBST for 10 min, the membranes were developed for 4 min with SuperSignal substrate (34076, ThermoFisher) and imaged on an iBright Imaging System (Invitrogen). For all incubation and washing steps, the membranes were placed on a rocker. Western blots were quantified by using ImageJ. The relative protein density for each condition was normalized by the relative density of the loading controls and again normalized with respect to the scramble CRISPR control condition.

Intracranial tumour injection

First, anesthetized 7-week-old female nude mice (NCRNU, Taconic Biosciences) were immobilized in a stereotaxic apparatus. After performing a small incision along the scalp, the skin was retracted, and a small hole was drilled into the skull to allow space for the injection needle. Next, a 26-gauge Hamilton syringe was placed at the 1.5 mm medial–lateral, 1.3 mm anterior–posterior and 3 mm dorsal–ventral stereotactic coordinates and, after a few seconds, retracted to a 2.5 mm dorsal–ventral depth to create space. Then, 2 µl of 1205Lu cells at 100,000 cells per microlitre suspended in L-15 basal medium (11415-064, Gibco) were injected at 0.25 µl min^{-1}. Three minutes after the injection was completed, the syringe was slowly retracted, bone wax (Kwik-Sil, WPI) was applied to the drilled hole and surgical adhesive (Vetbond, B00016067, 3M) was used to close the incision site. One week after the injections, brains were dissected after cardiac perfusion of 4 ml of 4% PFA in PBS+ and fixed overnight at 4 °C. After washing the brains once with PBS+, they were sliced into 300 µm sections and stained as described in previous sections. Tumours spanned through four to seven slices. The mounted slices were imaged on an upright Leica TCS SP8 confocal microscope. For each slice, a region containing the tumour section of 100 µm in depth was imaged and analysed. The volume was approximated for each tumour slice by multiplying the area of a maximum projection of the tumour by the slice thickness (300 µm). The roughness ratio was calculated in one single plane per slice as the ratio between the length of the real boundary of the tumour and a sharp boundary around the tumour edge (excluding the branches; Extended Data Fig. 5).

Microfluidic device fabrication

The devices were fabricated using soft lithography as previously described[33]. In short, PDMS (Sylgard184, Dow Corning) was mixed at a standard ratio of 1:10 (w/w) of PDMS base to crosslinking reagent. This mixture was poured over plastic copies of a silicon master wafer (with positive relief structures of the device shape), degassed in a vacuum chamber until bubbles dissipated and cured overnight

in a 60 °C oven. This PDMS was removed from the mould and cut into individual devices. A 2 mm biopsy punch (33-31, Integra Lifesciences) was used to form the sites for gel injection (gel ports) and a 5 mm biopsy punch (33-35, Integra Lifesciences) was used to make the medium reservoirs. PDMS devices were then bonded to cover glass by activation of the surface via plasma treatment at 100 W for 30 s. Bonded devices were incubated in a 100 °C oven for 30 min. To surface treat devices, they were plasma treated at 100 W for 30 s (glass side down), filled with 0.01% poly-L-lysine (P8920, Sigma) through the gel ports for at least 4 h (ensuring that the entire gel region is wet and does not dry out by placing devices in a parafilm-sealed 15 cm plastic dish), washed with MiliQ water, dried and filled with 1% glutaraldehyde (16310, EMS) for 15 min. Finally, they were washed and soaked overnight in MiliQ. After removing water from the devices, they were washed with 96% ethanol and dried. Steel acupuncture needles (160 µm diameter, SJ10.16 × 30, Seirin) were introduced into each device, and devices were ultraviolet sterilized for 15 min.

To prepare a 250 µl mix of a 3 mg ml^{-1} collagen type I solution, we mixed (on ice) 31 µl of diH_2O, 25 µl of M199 10× (M0650, Sigma), 10 µl of a 250 mM HEPES solution, 7 µl of a $NaHCO_3$ 1.25% solution, 171 µl of collagen-I (4.39 mg m^{-1}; 354236, Corning) and 6 µl of NaOH 1 M (SS256, Fisher; to achieve a pH of 7.5). Then, 225 µl of the 3 mg ml^{-1} collagen-I solution were mixed with 60 µl of 1% thiol-modified HA solution (HyStem Kit, GS311, AdvancedBiomatrix) and 15 µl of 2% PEG diacrylate solution (PEGDA, GS3006, AdvancedBiomatrix). Approximately 35 µl of the gel mix were added per device through the gel ports, and the devices were transferred to an incubator. After 1.5 h (or after 1 h if the gel contained cancer cells), EGM2-MV medium was added on top of each device (covering gel and medium ports). After 5 h, the needles were removed, needle guides were blocked with vacuum grease (Dow Corning) to avoid leakage and the medium was changed to only fill medium ports. The devices were then transferred to 10 cm plastic dishes for easier handling and incubated on a rocker at 37 °C overnight. To maintain humidity within the devices, we added wet tissues inside the dish (following the borders).

Microfluidic device cell seeding

For all experiments, EGM2-MV medium was used for culturing cells in devices. To compare cell shape differences between cells in the bulk and spreading along the vessel, 20,000 cancer cells per device were incorporated in the collagen–HA gel and incubated overnight. The following day, the brain endothelial cells were seeded in the channel. For all other experiments, the cancer cells were seeded on the channel, allowed to attach on an incubated rocker for 3 h before seeding endothelial cells. The seeding of cells in the channel was performed as previously described[33]. First, the medium was removed from medium reservoirs and gel ports (to avoid damaging the gel, the medium was removed from gel ports using a 10 µl pipette). Then, medium containing 0.5 million HMBECs per millilitre or 50,000 cancer cells per millilitre was added to medium reservoirs (45 µl to one reservoir and 50 µl to the other, to allow cells to flow into the channel). The devices were seeded for approximately 2 min (devices were flipped upside down after 1 min to seed the channel top surface). To maintain vessel health, the cancer cells were seeded very sparsely. The medium was replaced after seeding, and the devices were incubated on a rocker at 37 °C, replacing the medium every 24 h. Culturing devices on a rocker provided an oscillatory flow that had previously been shown to strengthen endothelial cell–cell junctions and enhance barrier function[33]. The devices were fixed after 2 days in culture.

BME experiment

BME coating. A 1:100 dilution of BME (3433-001-01, Cultrex) in PBS was added to the medium reservoirs. The devices were placed on a rocker at 37 °C for 2 h before seeding cancer cells.

BME gel. A total of 3 h after seeding cancer cells, the medium was replaced with cold medium, and the devices were placed on ice for 5 min. For six devices, a mixture of 450 µl of BME, 150 µl of cold medium and 3.6 µl of red fluorescent beads (F8812, ThermoFisher) was prepared on ice. After removing the medium from the reservoirs (and not from the gel ports), 40 µl of the gel mix was added to one reservoir and 50 µl to the other reservoir to allow the BME to flow into the channel. The devices were left at room temperature for 5–10 min until the gel was polymerized and then transferred to an incubator (static).

iCasp9–GFP experiment

After 24 h in culture, the medium was replaced from devices by adding either 5 nM CID (635060, TakaraBio) medim or ethanol control medium. The devices were transferred to an incubator (static) and fixed 12 h later. For all staining steps, the devices were kept static to prevent damaging the endothelial cell-deposited ECM in the channel.

Myosin-KO experiment

For each experiment, HMBEC LifeAct–Ruby (p5) cells were infected with either scramble CRISPR control or myosin-IIa CIRSPR lentivirus 6 days before seeding devices. Three days before seeding, the cells were passed and selected with 2 µg ml^{-1} puromycin (A1113803, Gibco). The cells were divided into three different plates: one for western blot, one for seeding devices and one for nano-indentation.

Sphericity calculation

The cancer cell sphericity was calculated using a custom-made MATLAB software. LifeAct image *z* stacks of cells were binarized by defining a proper threshold, and the properties of the 3D shape (including cell sphericity) were computed.

Device time-lapse microscopy and velocity measurements

Multi-dimensional acquisitions of devices were performed on an automated inverted microscope (Nikon EclipseTi) equipped with thermal and CO_2 control, using the MetaMorph software. The images were obtained every 30 min overnight. The mean cell velocities of individual cells moving along the micro-vessels were computed using the TrackMate plugin in ImageJ[64].

Microfluidic device staining

The devices were fixed with 4% PFA in PBS+ for 15 min at 37 °C. The devices were then washed three times with PBS+ for 5 min and blocked with 2% bovine serum albumin (BSA; A9647, Sigma) in PBS+ for at least 1 h. The primary antibodies were incubated overnight in 2% BSA in PBS+ at 4 °C and washed five times for 20 min with PBS+ at room temperature the following day. The secondary antibodies were incubated for 3 h at room temperature in 2% BSA in PBS+ and then washed several times with PBS+. If required, during one of the washing steps, the devices were incubated with a 1:5,000 Hoechst solution in PBS for 20 min. For all steps, the devices were placed on a rocker. The devices were imaged on an upright Leica TCS SP8 confocal microscope.

Antibodies

For immunostaining, the primary antibodies used were laminin rabbit antibody (ab11575, Abcam; 1:1,000 concentration for brain slices and 1:500 for devices), p-paxillin rabbit antibody (2541S, Cell Signaling; 1:100 concentration) and anti-GFP chicken antibody (ab13970, Abcam; 1:500 concentration, used for the B16-F10 cells). The secondary antibodies used were Alexa Fluor Plus 647 anti-rabbit (A32795, ThermoFisher; 1:500 concentration for laminin and 1:200 for p-paxillin) and Alexa Fluor Plus 488 anti-chicken (A32931, ThermoFisher; 1:500 concentration).

For western blots, the primary antibodies used were β-actin rabbit antibody (4970S, Cell Signaling; 1:5,000 concentration), CD44 mouse

antibody (3570T, Cell Signaling; 1:1,000 concentration), recombinant integrin β1 antibody (ab134179, Abcam; 1:1,000 concentration), zyxin rabbit antibody (PA5-78236, ThermoFisher; 1:1,000 concentration), paxillin mouse antibody (AHO0492, ThermoFisher; 1:1,000 concentration), talin 1 mouse antibody (MCA4770GA, BioRad; 1:1,000 concentration), talin 2 mouse antibody (NBP2-50322, Novus; 1:1,000 concentration) and vinculin mouse antibody (V9131, Sigma; 1:1,000 concentration). The secondary antibodies used were anti-mouse horseradish peroxidase (HRP)-linked antibody (7076S, Cell Signaling; 1:1,000 concentration) and anti-rabbit HRP-linked antibody (7074S, Cell Signaling; 1:1,000 concentration).

Nano-indentation and AFM

Nano-indentation measurements were performed using a Piuma nano-indenter system (Optics11). A 52 µm radius, 0.22 N m^{-1} stiffness probe was used for dextran gels, a 2.5 µm radius, 0.29 N m^{-1} stiffness probe was used for endothelial cell stiffness measurements and a 3 µm radius, 0.023 N m^{-1} stiffness probe was used for brain tissue and collagen–HA gel measurements. Young's elastic modulus was estimated using the Hertz model, with a 0.5 Poisson's ratio.

Cryosectioning of brains from 7- to 17-week-old male and female Tg(TIE2GFP)287Sato and FVB/NJ mice (003658 and 001800, Jackson Laboratory) brains was performed at the Koch Institute Histology Core. The fresh brains were embedded in an optimum cutting temperature embedding medium (OCT, 4585, Fisher) within a disposable plastic base mould (18986-1, Polysciences) that was placed on top of dry ice for ~5–10 min for the OCT to harden around the tissue, then stored at −80 °C until cryosectioned. Before performing the stiffness measurements, frozen 20 µm brain tissue sections were fast thawed by immersion in PBS at room temperature for 5 min. To label the vasculature, the sections were immersed in a 20 µg ml^{-1} solution of isolectin GS-IB4 (I21411, ThermoFisher) in PBS for 20 min. The samples were then washed once with PBS and transferred to the AFM. Indentations were performed using an MFP3D-BIO inverted optical AFM (Asylum Research) mounted on a Nikon TE2000-U inverted fluorescent microscope. Silicon nitride cantilevers were used with a spring constant of 0.06 N m^{-1} and a borosilicate glass spherical tip with 5 µm diameter (NovascanTech). Young's elastic modulus was estimated using the Hertz model, with a 0.5 Poisson's ratio.

The mechanical properties of alginate hydrogels were measured using a JPK NanoWizard AFM (Bruker) and a SAA-SPH-5UM cantilever with a spherical tip of 5 µm radius and a spring constant of 0.152 N m^{-1} (Bruker). Young's elastic modulus was estimated using the Hertz model, with a 0.5 Poisson's ratio, using the JPK Data Processing software.

Dextran methacrylate chemical synthesis

To synthesize dextran methacrylate, 2 g of dextran (molecular weight (MW) of 86 kDa; 205195, MPBiomedicals) was dissolved in 10 ml anhydrous dimethyl sulfoxide (276855, Sigma) with 0.2 g of base catalyst 4-dimethylamino pyridine (522821, Sigma) and 2.5 ml glycidyl methacrylate (density of 1.042 g ml^{-1} at 25 °C; 779342, Sigma). The solution was kept constant at 45 °C and stirred for 24 h before pipetting the dark brown reaction drop by drop into 100 ml of ice-chilled isopropanol to precipitate the final product. The isopropanol solution was collected in 50 ml tubes and centrifuged at 20,000*g* for 5 min at 4 °C. After centrifugation, isopropanol was discarded, and the pellets were resuspended in MiliQ water (around 35 ml per tube) and dialysed against 4 litres of milli-Q water at 4 °C for 3 days with three changes daily before lyophilization. Purified methacrylate–dextran was stored at −20 °C until use. The degree of methacrylation was determined via nuclear magnetic resonance spectroscopy (Extended Data Fig. 8g) and calculated as the ratio between the averaged peak area of the protons at the double bond (5.86 ppm and 6.31 ppm) and the peak area of the anomeric proton (5.07 ppm), yielding a 73% functionality (73 conjugated methacrylate groups per 100 dextran glucopyranose residues).

Dextran cardiac perfusion

Male and female FVB/NJ 7–17-week-old mice (001800, Jackson Laboratory) were used for this experiments. Dextran methacrylate gels were perfused into the brain vasculature using a protocol adapted from a previous publication[65]. The day before perfusion, dextran methacrylate was dissolved at 100 mg ml^{-1} in M199 1×, brought to pH 8 by adding NaOH 1 M, labelled with TAMRA (tetramethylrhodamine)-thiol (KWT1057, BioActs) and frozen at −20 °C until the following day. To label dextran, 17.3 µl of 1 mM TAMRA were added per millilitre of dissolved dextran (pH 8) and the mix was protected from light at room temperature for 1 h before freezing. Right before perfusion, a four-arm PEG-thiol 2 kDa crosslinker (PSB-440, CreativePEGWorks) was dissolved in PBS+ and brought to pH 8 with small amounts of NaOH 1 M. The mice were anesthetized with isoflurane. Using a peristaltic pump (Ismatec; at 4 ml min^{-1}) and a 23-gauge needle (367297, BD), through cardiac perfusion, all mice were perfused 12 ml of NMDG buffer supplemented with 0.02 mg ml^{-1} heparin (Celsus) and 0.4 mg ml^{-1} verapamil (329330010, ThermoFisher) to flush out the blood. Afterwards, control animals were perfused 4.5 ml of a 20 µg ml^{-1} solution of isolectin GS-IB4 (I21412, ThermoFisher) in PBS, soft dextran animals were perfused with 4.5 ml of a 2.2% dextran and 7.7% crosslinker mix and stiff dextran animals were perfused with 4.5 ml of a 5.7% dextran and 20.3% crosslinker mix. Dextran and crosslinker solutions were mixed gently to avoid bubbles immediately before the mix was perfused. A sample of the gel mix was transferred during perfusion to a separate dish for nano-indentation. All solutions were filtered with a 0.2 µm filter (431224, Corning) and degassed before perfusion (the dextran methacrylate and crosslinker solutions were filtered separately before mixing them). After the perfusion was complete, the brains were dissected and sliced as described in 'Brain slice culture'.

Alginate double-layered gel

Sodium alginate of average MW of 287 kDa (Protanal LF10/60, Dupont) was irradiated with a 5 Mrad cobalt source to obtain an average MW of 57 kDa and conjugated to the adhesion peptide GGGGRGDSP as previously described[66]. To encapsulate 1205Lu LifeAct–GFP cells between alginate hydrogels, a first gel containing 3% alginate–RGD (arginine-glycine-aspartic acid) and 1 mg ml^{-1} Cultrex BME (3533-010-02, Bio-techne) was made. Briefly, alginate–RGD, BME, red fluorescent beads (0.2 µm, F8810, Invitrogen) and culture media were mixed on ice. An initial slurry of 10% calcium carbonate ($CaCO_3$, Mineral Technologies, Multifex-MM) was made by dissolving 100 mg ml^{-1} $CaCO_3$ in water, and the appropriate amount of solution was added to each gel preparation so that the final amount of $CaCO_3$ was 0.2% in soft gels, 0.9% in stiff gels for experiments in Fig. 5 and 0.53% in stiff gels for experiments in Extended Data Fig. 8. Polymerization was then induced by addition of freshly dissolved D-(+)-glucono-delta-lactone (GDL) (G4750, Sigma Aldrich) at 400 mg ml^{-1} in PBS with 20 mM HEPES (15630056, Gibco), using a 4× molar excess of the calcium concentration. The gels were dispensed in a glass-bottom six-well plate (P06G-1.5-20-F, MatTek). After 1 h polymerization at 37 °C, 10,000 cells were added in 10 µl on each gel and left to attach for 2 h at 37 °C with 5% CO_2. Finally, a second gel containing 3% alginate (no RGD and no BME) was made on top of the cells and left to polymerize for 1 h at 37 °C. The top gels were made with far-red fluorescent beads (0.2 µm, F8807, Invitrogen). The culture medium was then added to the wells and changed after 1 h and 4 h. The following day, the medium was changed again, and the cells were imaged every 20 min for 18 h at 37 °C and 5% CO_2 using an automated inverted spinning-disk microscope (Nikon Eclipse Ti2) using NIS Element software. The cells were tracked using the TrackMate plugin in Fiji[64], and the mean cell speed was used to quantify cell movement. Only tracks longer than 80 min were kept for analysis.

Statistics and reproducibility

Experimental data were analysed and processed in MATLAB and ImageJ and plotted using GraphPad Prism software. No statistical method was used to predetermine sample size. The number of experiments, sample size and statistic tests are reported in the figure legends. To choose the appropriate statistical test, normality tests were performed for all datasets. No data were excluded from the analyses. The experiments were not randomized. The investigators were not blinded to allocation during experiments and outcome assessment.

Reporting summary

Further information on research design is available in the Nature Portfolio Reporting Summary linked to this article.

Data availability

All data supporting the findings of this study are available from the corresponding author on reasonable request. Source data are provided with this paper.

Code availability

Code use in this article can be made available upon request to the corresponding author.

References

60. Debnath, J. et al. The role of apoptosis in creating and maintaining luminal space within normal and oncogene-expressing mammary acini. *Cell* **111**, 29–40 (2002).
61. Mishra, A. et al. Imaging pericytes and capillary diameter in brain slices and isolated retinae. *Nat. Protoc.* **9**, 323–336 (2014).
62. Segel, M. et al. Niche stiffness underlies the ageing of central nervous system progenitor cells. *Nature* **573**, 130–134 (2019).
63. Qi, L. et al. Talin2-mediated traction force drives matrix degradation and cell invasion. *J. Cell Sci.* **129**, 3661–3674 (2016).
64. Ershov, D. et al. TrackMate 7: integrating state-of-the-art segmentation algorithms into tracking pipelines. *Nat. Methods* **19**, 829–832 (2022).
65. Miyawaki, T. et al. Visualization and molecular characterization of whole-brain vascular networks with capillary resolution. *Nat. Commun.* **11**, 1104 (2020).
66. Elosegui-Artola, A. et al. Matrix viscoelasticity controls spatiotemporal tissue organization. *Nat. Mater.* **22**, 117–127 (2023).

Acknowledgements

We thank L. Kelleher for technical assistance; R. Alani for providing 1205Lu, B16-F10 and WM983B cells; H. T. Nia for providing E0771 cells; the Memorial Sloan Kettering Cancer Center for providing the MDA cell lines; J. L. Teo, H.-S. Li and W. W. Wong for providing T cells; C. Stashko for his assistance during the AFM measurements; and J. A. White for giving us access to their vibratome. We also thank the Bio-Interface and Technology core facility at Boston University (used for nano-indentation) and the Koch Institute histology core (used for tissue cryosectioning). This work was supported by grants from the National Institutes of Health (NIH) (EB033821) and the National Science Foundation (NSF) Center for Engineering MechanoBiology (CMMI-1548571). M.U. was supported by an European Molecular Biology Organization long-term fellowship (EMBO ALTF811-2018), the Center for Multiscale and Translational Mechanobiology at Boston University and an American Heart Association postdoctoral fellowship (828475). A.E.S. was supported by an NSF Graduate Research Fellowship (1745302 and 2141064) and a Boston University Multicellular Design Program Kilachand Fellowship. B.P.S. was supported by the NIH National Institute of Biomedical Imaging and Bioengineering (no. T32 EB016652). R.O. was supported by an NIH R35 (CA242447-01). C.R.R. was supported by an NSF Graduate Research Fellowship (2021324226). J.B.T. was supported by the NIH through the Translational Research in Biomaterials Training Program (no. T32 EB006359). M.T.N. was supported by an NIH NRSA F32 postdoctoral fellowship (NIH NHLBI 1F32HL165691). J.E. acknowledges support from the NIH (R21 EB28491). A.E.A. acknowledges the support from the European Research Council (ERC) under the European Union's Horizon 2020 research and innovation programme (grant agreement number 851055). A.E.A. is supported by the Francis Crick Institute, which receives its core funding from Cancer Research UK (CC2214), the UK Medical Research Council (CC2214) and the Wellcome Trust (CC2214).

Author contributions

M.U. and C.S.C. conceived the study and designed the experiments. M.U., A.E.S., B.P.S., O.C., R.O., C.R.R., L.L, M.T.N., J.B.T. and J.Y. performed the experiments. M.U. and O.C. analysed the data. R.O. and V.M.W. oversaw the AFM data collection. O.C. and A.E.A. designed alginate gel experiments. C.R.R. and X.H. performed and oversaw brain injections. J.E. contributed to data interpretation. All authors discussed results. M.U., J.E. and C.S.C. wrote the manuscript with feedback from all authors. C.S.C. oversaw the project.

Competing interests

The authors declare no competing interests.

Additional information

Extended data is available for this paper at https://doi.org/10.1038/s41556-024-01532-6.

Supplementary information The online version contains supplementary material available at https://doi.org/10.1038/s41556-024-01532-6.

Correspondence and requests for materials should be addressed to Christopher S. Chen.

Peer review information *Nature Cell Biology* thanks Steven D. Chang, Gregory Longmore and the other, anonymous, reviewer(s) for their contribution to the peer review of this work. Peer reviewer reports are available.

https://doi.org/10.1038/s41556-024-01532-6

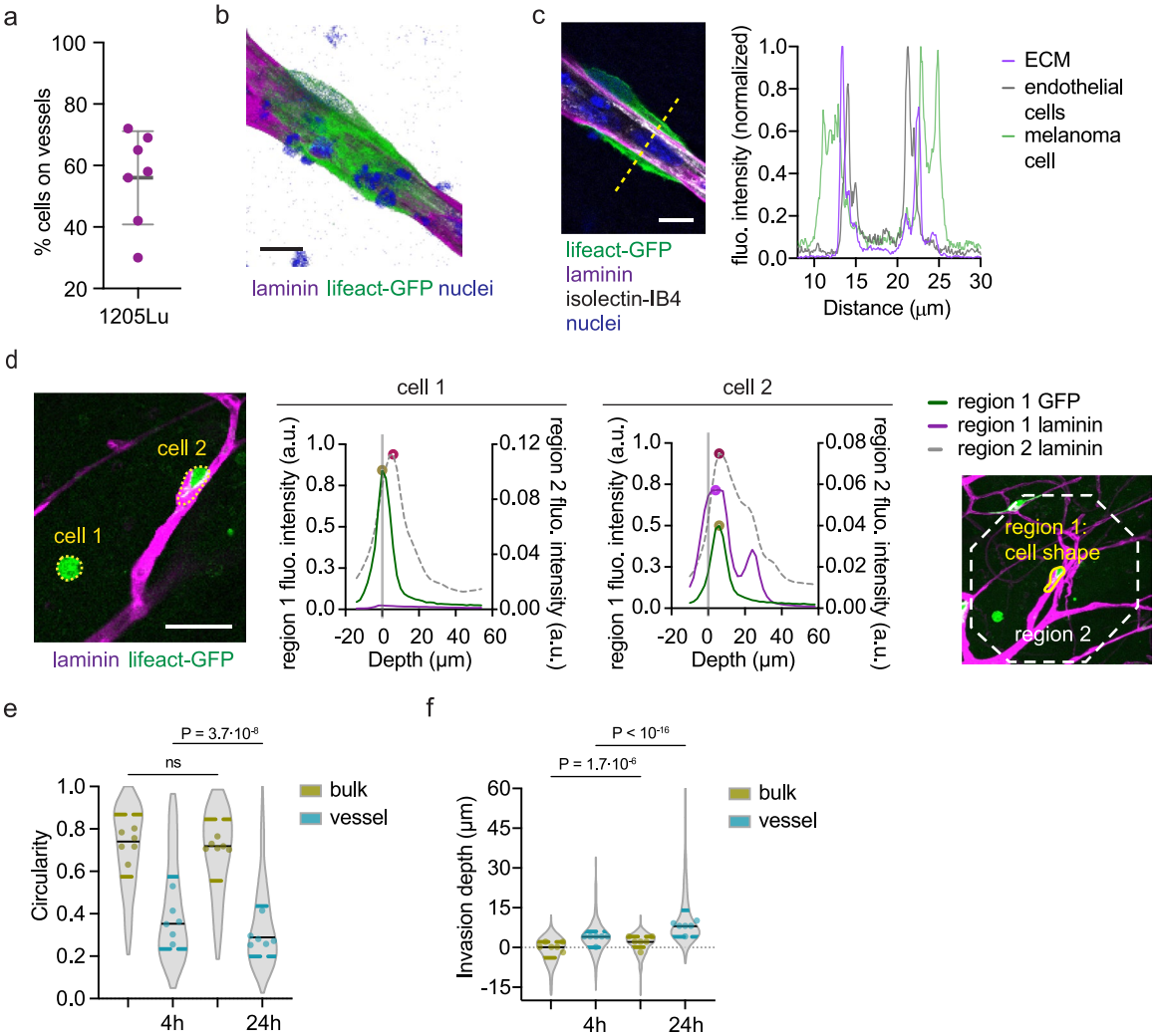

Extended Data Fig. 1 | Characterization of cell shape and invasion depth in *ex vivo* brain cultures. (**a**) Percentage of 1205Lu cells adhered to vessels after 24h of *ex vivo* culture (n=7 slices, 4 experiments). Graph shows mean ± standard deviation. (**b**) Brain slice immunostaining of laminin (magenta), lifeact-GFP (green) and nuclei (hoechst, blue) of a 1205Lu cell spreading over the outer surface of a vessel. 3D view,11μm-thick image stack. Scale bar 10μm. (**c**) Left: single image plane of the cell in (b), including isolectin-IB4 labelling of endothelial cells (grey). Scale bar 10μm. Right: laminin (magenta), lifeact-GFP (green) and isolectin-IB4 (grey) fluorescence profile along the dashed yellow line. (**d**) Example of cell invasion depth quantification. Left: immunostaining of laminin (magenta) and lifeact-GFP (green). Yellow dashed lines outline a cell in the bulk (cell 1) and a cell spreading along a vessel (cell 2). Scale bar 50μm. Right: region 2 (centred on the cell of interest) is used to average laminin intensity across a 60μm stack and define the reference point for invasion depth (0μm). Because of the opacity of brain tissue, averaged laminin intensity shows a peak at the top of the slice and decays as imaging deeper into the tissue. The origin of invasion depths is defined as $z_{peak\_region2} - 6\mu m$. Region1 (that follows the cell 2D shape), is used to average both cell and laminin fluorescence. The intensity of the GFP signal is used to determine the cell depth within the slice, and local laminin intensity is used to determine if a cell is in the bulk or on a vessel (if observing a local peak of laminin intensity). (**e**) Violin plots of 1205Lu cell shape circularities when adhered to vessels or to the bulk brain tissue 4 and 24h after seeding. (**f**) Violin plots of 1205Lu invasion depths within the slice when adhered to vessels or to the bulk brain tissue 4 and 24h after seeding. For e-f, n=562 for Bulk, n=621 for Vessel at 4h, n=337 for Bulk, n=706 for Vessel at 24h, from 6 slices, 3 experiments. Graphs show median ± interquartile range. Dots represent the median values for each slice analysed. Statistical analysis: Kruskal–Wallis test followed by a post hoc Dunn's test.

https://doi.org/10.1038/s41556-024-01532-6

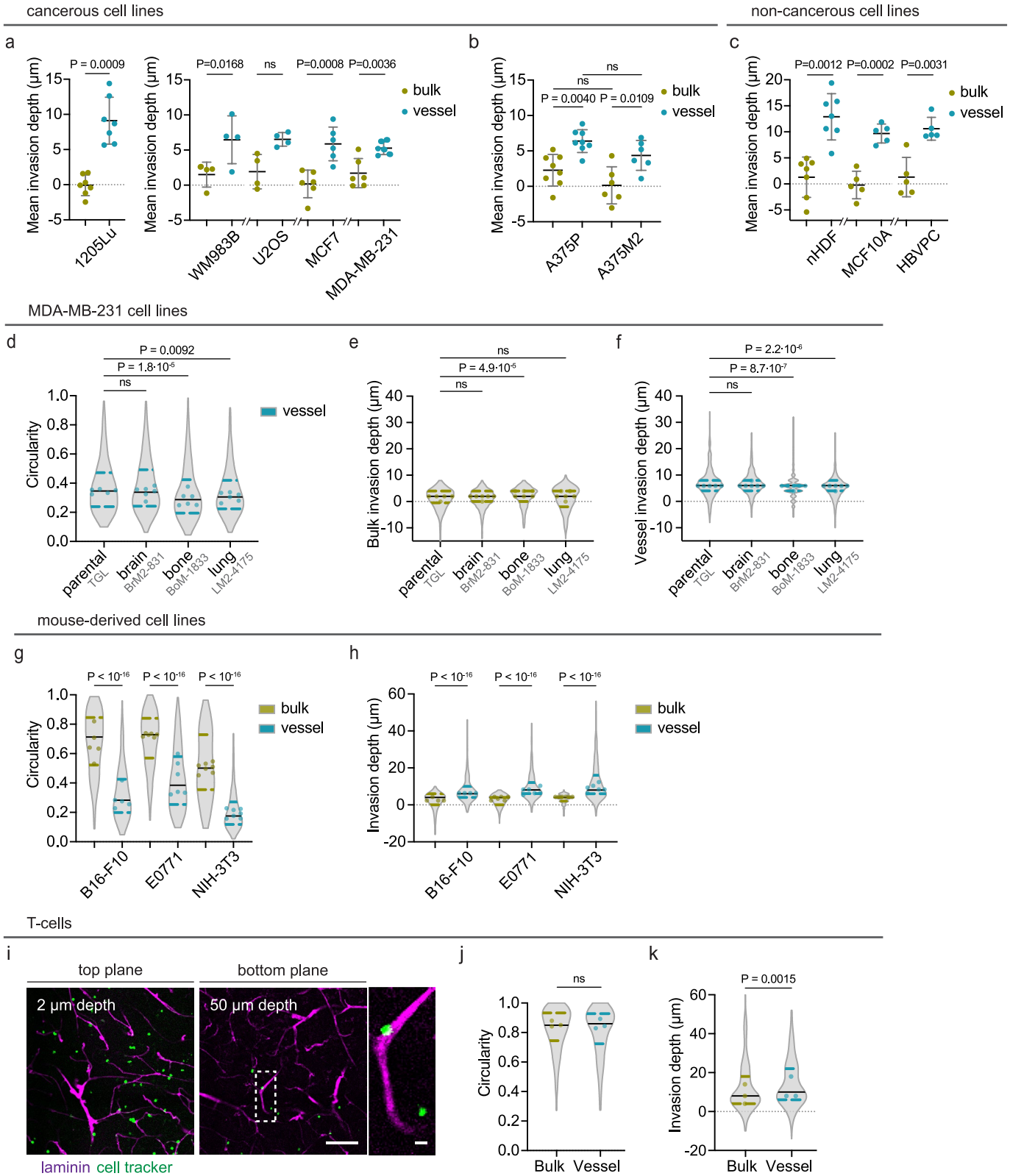

Extended Data Fig. 2 | See next page for caption.

https://doi.org/10.1038/s41556-024-01532-6

Extended Data Fig. 2 | Vessel co-option is a common pattern of invasion across many different cell lines. a-c, Mean invasion depth per slice for cells adhered to vessels or to the bulk brain tissue for 1205Lu (n=7), WM983B (n=4), U2OS (n=4), MCF7 (n=6) and MDA-MB-231 (n=6) (**a**), A375P (n=8) and A375M2 (n=6) (**b**), nHDF (n=7), MCF10A (n=5) and HBVPC (n=5) cell lines (**c**). Full distributions shown in Fig. 1d, j–l. Data corresponds to at least 3 experiments. Statistical analysis: two-sided paired T-test or an ordinary one-way ANOVA test followed by a post hoc Tukey's test (for b). All graphs show mean ± standard deviation. (**d**) Violin plots of cell shape circularities for MDA-MB-231 TGL, BrM2-831, BoM-1833 and LM2-4175 cells adhered to the vasculature. (**e**) Violin plots of bulk invasion depths for MDA-MB-231 TGL, BrM2-831, BoM-1833 and LM2-4174 cells. (**f**) Violin plots of vessel invasion depths for MDA-MB-231 TGL, BrM2-831, BoM-1833 and LM2-4175 cells. (**g**) Violin plots of cell shape circularities for cells adhered to vessels or to the bulk brain tissue for B16-F10, E077 and NIH-3T3 mouse-derived cell lines. (**h**) Violin plots of invasion depths for cells adhered to vessels or to the bulk brain tissue for B16-F10, E0771 and NIH-3T3 mouse-derived cell lines. For MDA-MB-231 TGL (parental cell line): n=394 for Bulk, n=441 for Vessel, from 5 slices, 3 experiments. For BrM2-831 (brain tropic): n=652 for Bulk, n=479 for Vessel, from 6 slices, 3 experiments. For BoM-1833 (bone tropic): n=520 for Bulk, n=496 for Vessel, from 6 slices, 3 experiments. For LM2-4175 (lung-tropic): n=564 for Bulk, n=529 for Vessel, from 6 slices, 3 experiments. For B16-F10 (melanoma): n=239 for Bulk, n=212 for Vessel, from 4 slices, 3 experiments. For E0771 (breast cancer): n=269 for Bulk, n=359 for Vessel, from 6 slices, 3 experiments. For NIH-3T3 (embryonic fibroblast): n=165 for Bulk, n=530 for Vessel, from 6 slices, 3 experiments. (**i**) Brain slice immunostaining of laminin (magenta) and T-cells labelled with CellTracker-488 (green). Left: z-plane 2µm below the top surface. Right: z-plane 50µm below the top surface. White insert labels zoomed area. Scale bars: 100µm, 10µm (inserts). (**j**) Violin plots of T-cell shape circularities when adhered to vessels or to the bulk brain tissue. (**k**) Violin plots of T-cell invasion depths within the slice when adhered to vessels or to the bulk brain tissue. For T-cells: n=380 for Bulk, n=208 for Vessel, from 3 slices, 2 experiments. For all violin plots, dots represent the median value for each slice analysed. Statistical analysis: two-sided Mann–Whitney or a Kruskal–Wallis test followed by a post hoc Dunn's test (for d-f). Graphs show median ± interquartile range.

https://doi.org/10.1038/s41556-024-01532-6

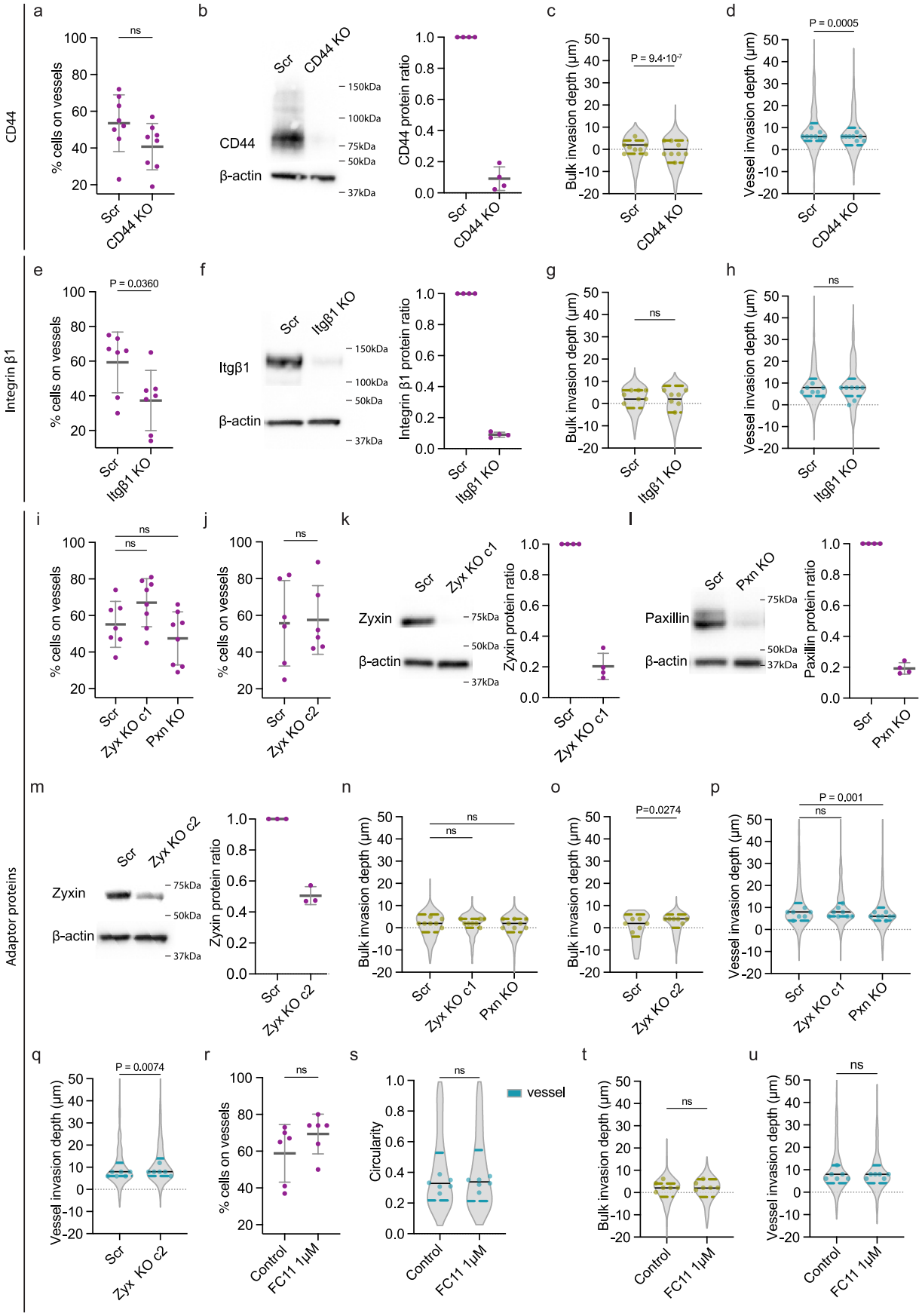

Extended Data Fig. 3 | See next page for caption.

https://doi.org/10.1038/s41556-024-01532-6

Extended Data Fig. 3 | Depletion of CD44, integrin β1, zyxin or paxillin does not significantly impair invasion into brain slices. (**a**) Percentage of scramble control and CD44 KO cells adhered to vessels after 24h of ex vivo culture (n=8 slices, 4 experiments). (**b**) Left: representative western blot of CD44 expression in scramble control and CD44 KO cells. Right: quantification of all western blots (one per experiment, 4 experiments). (**c**) Violin plots of invasion depths for scramble control and CD44 KO cells moving through the bulk brain tissue (Scr: n=571, CD44 KO: n=708, 8 slices, 4 experiments). (**d**) Violin plots of invasion depths for scramble control and CD44 KO cells moving along the vasculature (Scr: n=652, CD44 KO: n=511, 8 slices, 4 experiments). (**e**) Percentage of scramble control and integrin β1 KO cells adhered to vessels after 24h of *ex vivo* culture (n=7 slices, 4 experiments). (**f**) Left: representative western blot of integrin β1 expression in scramble control and integrin β1 KO cells. Right: quantification of all western blots (one per experiment, 4 experiments). (**g**) Violin plots of invasion depths for scramble control and integrin β1 KO cells moving through the bulk brain tissue (Scr: n=500, Itgβ1 KO: n=607, 7 slices, 4 experiments). (**h**) Violin plots of invasion depths for scramble control and integrin β1 KO cells moving along the vasculature (Scr: n=720, Itgβ1 KO: n=354, 7 slices, 4 experiments). **i-u**, Adaptor proteins. The zyxin CRISPR KO cell lines were established as clonal cell lines by single cell sorting after infection with the CRISPR lentivirus, and two cell lines were analysed (data shown in Fig. 2 corresponds to clone 1). (**i**) Percentage of scramble control, zyxin clone-1 KO and paxillin KO cells adhered to vessels after 24h of *ex vivo* culture (Scr: n=7 slices, Zyx KO c1: 8 slices, Pxn KO: 8 slices, 3 experiments). (**j**) Percentage of scramble control and zyxin clone-2 KO cells adhered to vessels after 24h of *ex vivo* culture (n=6 slices, 3 experiments). (**k**) Left: representative western blot of zyxin expression in scramble control and zyxin clone-1 KO cells. Right: quantification of all western blots (one per experiment, 4 experiments). (**l**) Left: representative western blot of paxillin expression in scramble control and paxillin KO cells. Right: quantification of all western blots (one per experiment, 4 experiments). (**m**) Left: representative western blot of zyxin expression in scramble control and zyxin clone-2 KO cells. Right: quantification of all western blots (one per experiment, 3 experiments). (**n**) Violin plots of invasion depths for scramble control, zyxin clone-1 KO and paxillin KO cells moving through the bulk brain tissue (Scr: n=467, 7 slices; Zyx KO c1: n=353, 8 slices; Pxn KO: n=660, 8 slices, 4 experiments). (**o**) Violin plots of invasion depths for scramble control and zyxin clone-2 KO cells moving through the bulk brain tissue (Scr: n=288 for Scr, Zyx KO c2: n=303, 6 slices, 3 experiments). (**p**) Violin plots of invasion depths for scramble control, zyxin clone-1 KO and paxillin KO cells moving along the vasculature (Scr: n=593, 7 slices; Zyx KO c1: n=704, 8 slices; Pxn KO: n=597, 8 slices, 4 experiments). (**q**) Violin plots of invasion depths for scramble control and zyxin clone-2 KO cells moving along the vasculature (Scr: n=275, Zyx KO c2: n=481, 6 slices, 3 experiments). **r-u**, FAK inhibition with FC11. (**r**) Percentage of cells adhered to vessels in control conditions or under 1μM FC11 after 24h of *ex vivo* culture (n=6 slices, 3 experiments). (**s**) Violin plots of cell shape circularities for cells adhered to the vasculature in control conditions or under 1μM FC11 (Control: n=631, FC11 1μM: n=642, 6 slices, 3 experiments). (**t**) Violin plots of invasion depths for cells moving through the bulk brain tissue in control conditions or under 1μM FC11 (Control: n=466, FC11 1μM: n=289, 6 slices, 3 experiments). (**u**) Violin plots of invasion depths for cells moving along the vasculature in control conditions or under 1μM FC11 (Control: n=631, FC11 1μM: n=642, 6 slices, 3 experiments). For all violin plots, dots represent the median values per slice analysed. Statistical analysis: two-sided Mann–Whitney or a Kruskal–Wallis test followed by a post hoc Dunn's test (for n,p). Graphs show median ± interquartile range. For all other graphs, statistical analysis was performed using a two-sided T-test or an ordinary one-way ANOVA test followed by a post hoc Tukey's test (for i). Graphs show mean ± standard deviation. For western blot quantification, protein expression was normalized to loading control (β-actin), and to the expression on the scramble control condition.

https://doi.org/10.1038/s41556-024-01532-6

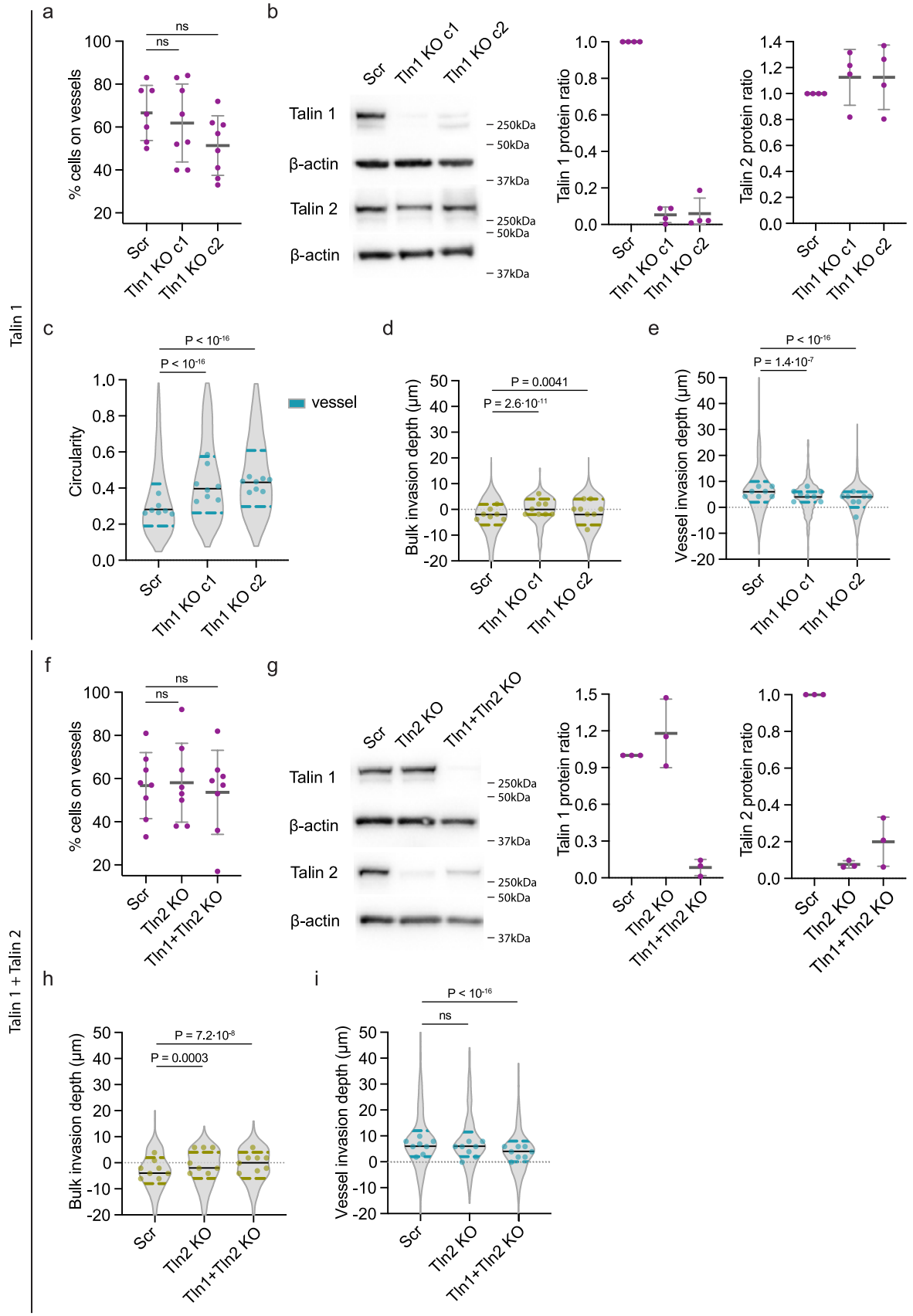

Extended Data Fig. 4 | See next page for caption.

https://doi.org/10.1038/s41556-024-01532-6

Extended Data Fig. 4 | Depletion of talin significantly impairs invasion into brain slices. a-e, Talin 1 KO. The talin 1 CRISPR KO cell lines were established as clonal cell lines by single cell sorting after infection with the CRISPR lentivirus, and two cell lines were analysed (data shown in Fig. 2 corresponds to clone 1). (**a**) Percentage of scramble control, talin 1 clone-1 KO and talin 1 clone-2 KO cells adhered to vessels after 24h of *ex vivo* culture (Scr: n=7, Tln1 KO: n=8, 4 experiments). (**b**) Left: representative western blot of talin 1 and talin 2 expression in scramble control, talin 1 clone-1 KO and talin 1 clone-2 KO cells. Right: quantification of all western blots (one per experiment, 4 experiments). (**c**) Violin plots of cell shape circularities for scramble control, talin 1 clone-1 KO and talin 1 clone-2 KO cells adhered to the vasculature (Scr: n=826, 7 slices; Tln1 KO c1: n=725, 8 slices; Tln1 KO c2: n=741, 8 slices; 4 experiments). (**d**) Violin plots of invasion depths for scramble control, talin 1 clone-1 KO and talin 1 clone-2 KO cells moving through the bulk brain tissue (Scr: n=425, 7 slices; Tln1 KO c1: n=521, 8 slices; Tln1 KO c2: n=721, 8 slices; 4 experiments). (**e**) Violin plots of invasion depths for scramble control, talin 1 clone-1 KO and talin 1 clone-2 KO cells moving along the vasculature (Scr: n=826, 7 slices; Tln1 KO c1: n=725, 8 slices; Tln1 KO c2: n=741, 8 slices; 4 experiments). **f-i**, Talin1+2 KO. (**f**) Percentage of scramble control, talin 2 KO and talin 1 and 2 KO cells adhered to vessels after 24h of *ex vivo* culture (n=8 slices, 4 experiments). (**g**) Left: representative western blot of talin 1 and talin 2 expression in scramble control, talin 2 KO and talin 1 and 2 KO cells. Right: quantification of all western blots (one per experiment, 4 experiments). (**h**) Violin plots of invasion depths for scramble control, talin 2 KO and talin 1 and 2 KO cells moving through the bulk brain tissue (Scr: n=560, Tln2 KO: n=509, Tln1+Tln2 KO: n=515, 8 slices, 4 experiments). (**i**) Violin plots of invasion depths for scramble control, talin 2 KO and talin 1 and 2 KO cells moving along the vasculature (Scr: n=717, Tln2 KO: n=640, Tln1+Tln2 KO: n=544, 8 slices, 4 experiments). For all violin plots, dots represent the median values per slice analysed. Statistical analysis: Kruskal–Wallis test followed by a post hoc Dunn's test. Graphs show median ± interquartile range. For all other graphs, statistical analysis was performed using a one-way ANOVA test followed by a post hoc Tukey's test. Graphs show mean ± standard deviation. For western blot quantification, protein expression was normalized to loading control (β-actin), and to the expression on the scramble control condition.

https://doi.org/10.1038/s41556-024-01532-6

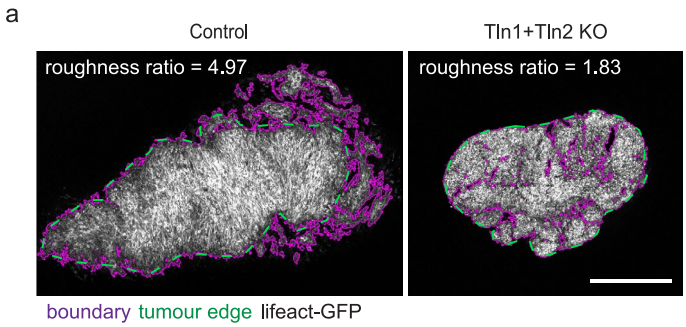

Extended Data Fig. 5 | Roughness ratio calculation. (**a**) 1205Lu lifeact-GFP image (grey). From left to right, representative images of a scramble control and a talin1 and 2 KO tumour one week after brain injection. Overlayed, the tumour edge (green) and boundary (magenta) that were used to calculate the roughness ratio as (boundary length)/(edge length). Scalebar 500μm.

https://doi.org/10.1038/s41556-024-01532-6

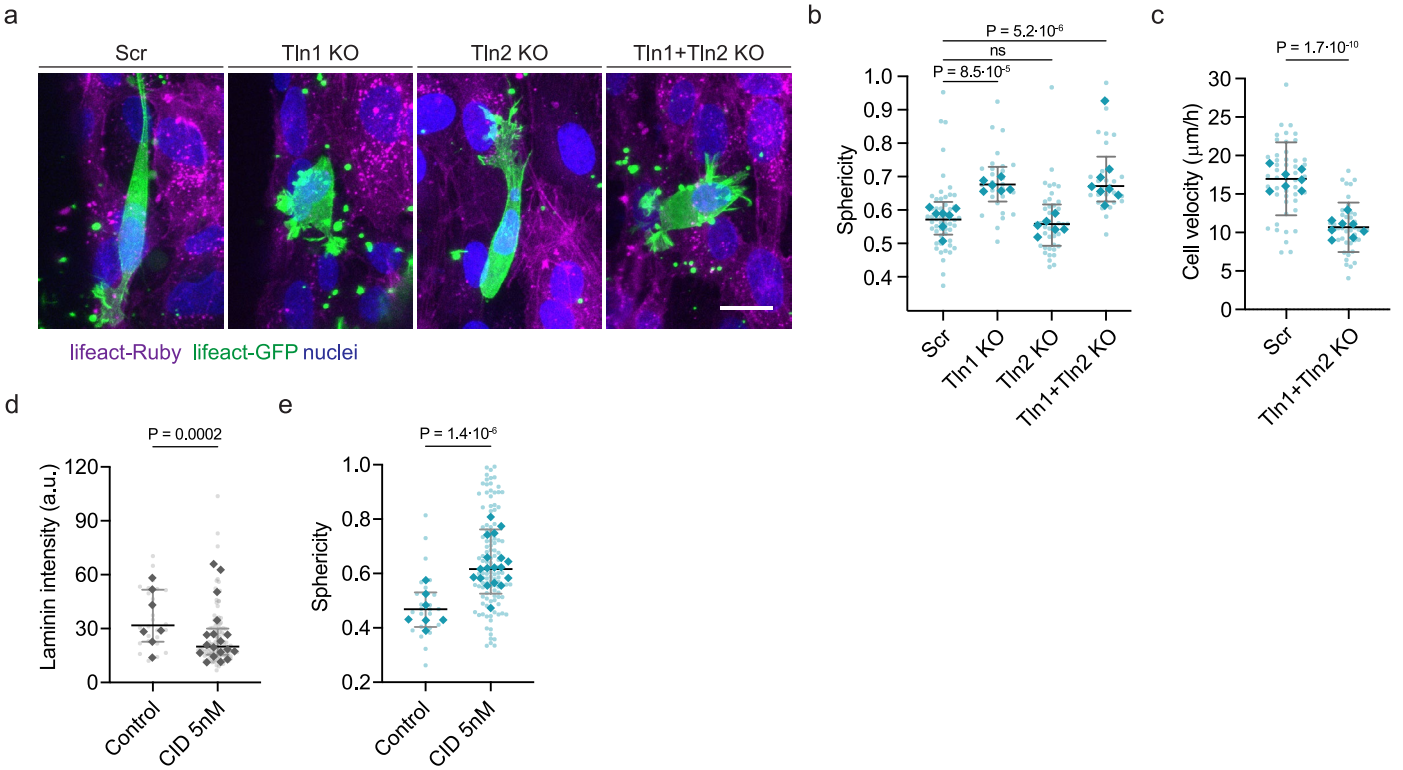

Extended Data Fig. 6 | Modelling vessel co-option *in vitro*. (**a**) Device immunostaining of HMBEC lifeact-Ruby (magenta), 1205Lu lifeact-GFP (green) and nuclei (hoechst, blue). From left to right, representative images of a scramble control, a talin 1 KO, a talin 2 KO and a talin 1 and 2 KO cell adhering to the micro-vessel. Maximum projection, scale bar 20µm. (**b**) Cell sphericity of scramble control, talin 1 KO, talin 2 KO and talin 1 and 2 KO cells adhered to the micro-vessel (Scr: n=53, 7 devices; Tln1 KO: n=25, 6 devices; Tln2 KO: n=42, 6 devices; Tln1+Tln2 KO: n=29, 8 devices; 3 experiments). Lighter dots represent each cell value and darker dots represent the median value per device. Statistical analysis: Kruskal–Wallis test followed by a post hoc Dunn's test. Graphs show median ± interquartile range. (**c**) Cell velocity of scramble control and talin 1 and 2 KO cells moving along the micro-vessel (Scr: n=47, 7 devices; Tln1+Tln2 KO: n=42, 8 devices; 3 experiments). Lighter dots represent each cell value and darker dots represent the mean value per device. Statistical analysis: two-sided T-test. Graph show mean ± standard deviation. **d-e**, Laminin intensity (**d**) and cell sphericity (**e**) of 1205Lu cells spreading on control devices or in devices where the apoptosis of endothelial cells was triggered with the small molecule CID (Control: n=26, 7 devices; CID 5nM: n=118, 18 devices; 4 experiments). Lighter dots represent each cell value and darker dots represent the median value per device. Statistical analysis: two-sided Mann–Whitney test. Graphs show median ± interquartile range.

https://doi.org/10.1038/s41556-024-01532-6

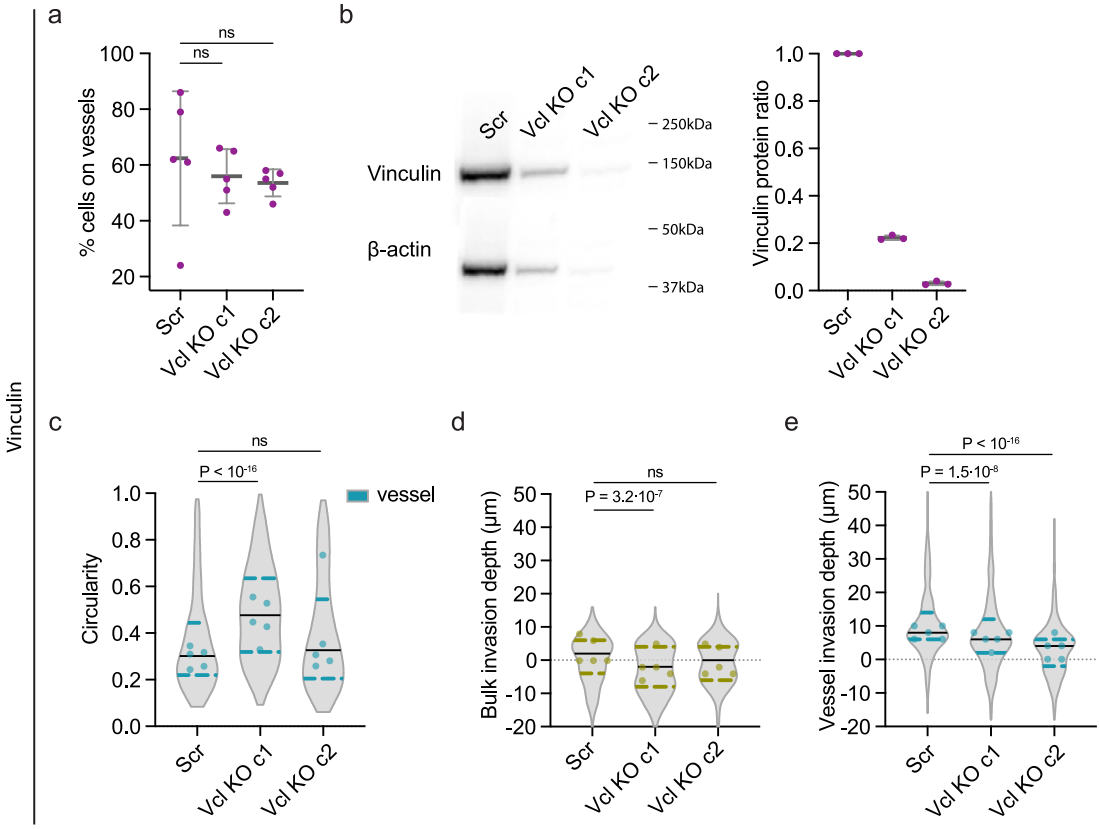

Extended Data Fig. 7 | Depletion of vinculin significantly impairs invasion into brain slices. The vinculin CRISPR KO cell lines were established as clonal cell lines by single cell sorting after infection with the CRISPR lentivirus, and two cell lines were analysed (data shown in Fig. 5 corresponds to clone 2). (**a**) Percentage of scramble control, vinculin clone-1 KO and vinculin clone-2 KO cells adhered to vessels after 24h of *ex vivo* culture (n=5, 3 experiments). Statistical analysis: one-way ANOVA test followed by a post hoc Tukey's test. Graphs show mean ± standard deviation. (**b**) Left: representative western blot of vinculin expression in scramble control, vinculin clone-1 KO and vinculin clone-2 KO cells. Right: quantification of all western blots (one per experiment, 3 experiments). (**c**) Violin plots of cell shape circularities for scramble control, vinculin clone-1 KO and vinculin clone-2 KO cells adhered to the vasculature (Scr: n=411, Vcl KO c1: n=453, Vcl KO c2: n=474, 5 slices, 3 experiments). (**d**) Violin plots of invasion depths for scramble control, vinculin clone-1 KO and vinculin clone-2 KO cells moving through the bulk brain tissue (Scr: n=242, Vcl KO c1: n=385, Vcl KO c2: n=411, 5 slices, 3 experiments). (**e**) Violin plots of invasion depths for scramble control, vinculin clone-1 KO and vinculin clone-2 KO cells moving along the vasculature (Scr: n=411, Vcl KO c1: n=453, Vcl KO c2: n=474, 5 slices, 3 experiments). For all violin plots, dots represent the median values per slice analysed. Statistical analysis: Kruskal–Wallis test followed by a post hoc Dunn's test. Graphs show median ± interquartile range. For western blot quantification, protein expression was normalized to loading control (β-actin), and to the expression on the scramble control condition.

https://doi.org/10.1038/s41556-024-01532-6

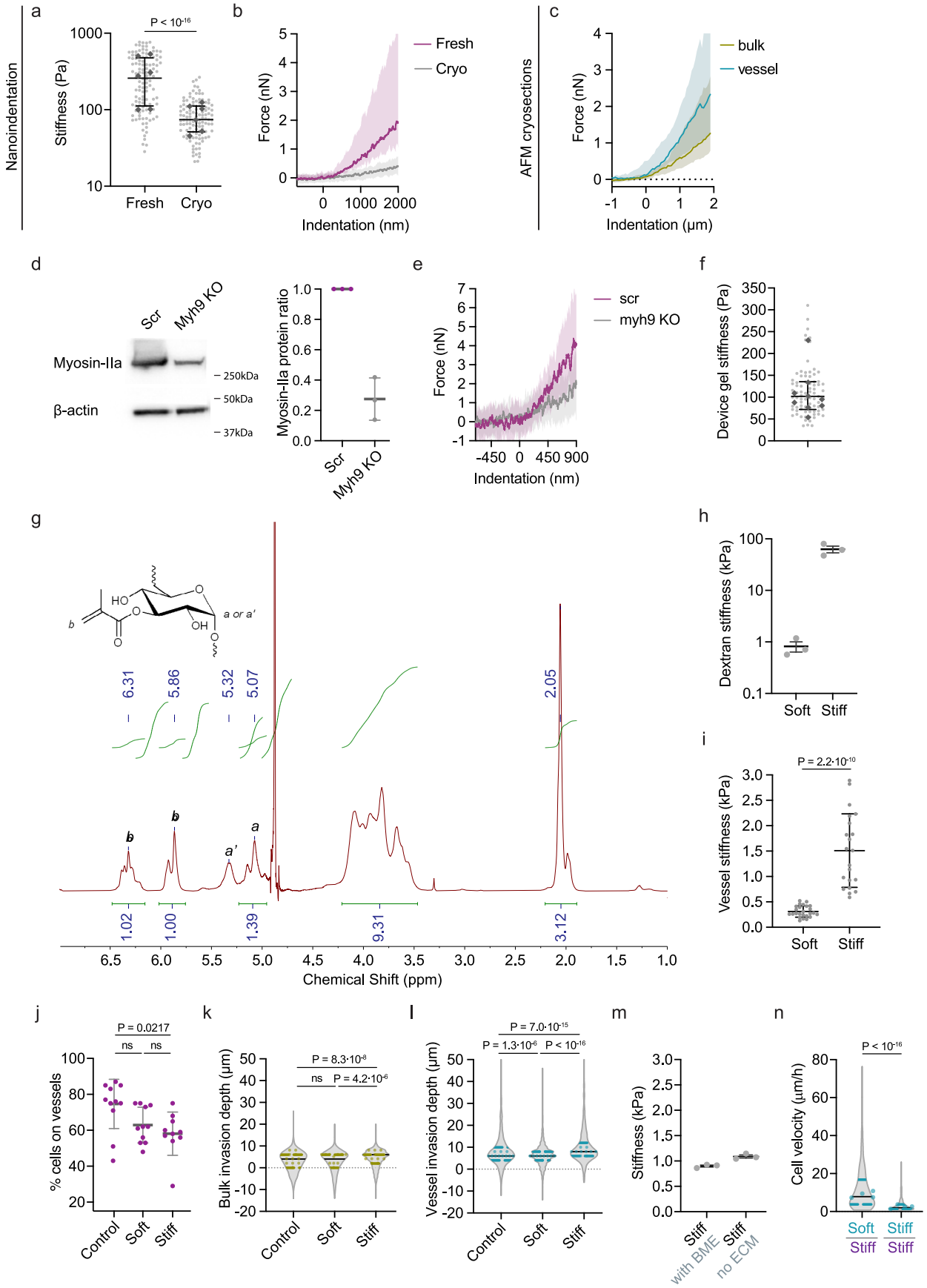

Extended Data Fig. 8 | See next page for caption.

https://doi.org/10.1038/s41556-024-01532-6

Extended Data Fig. 8 | Tuning the stiffness of the vasculature by filling it with a stiff gel or by inhibiting contractility. a-b, Brain stiffness characterization. Young's modulus (**a**) and force-indentation curves (**b**) of fresh 700µm-thick brain slices and 20µm-thick cryosections (Fresh: n=120, Cryo: n=120, 6 slices, 3 experiments). Statistical analysis: two-sided Mann–Whitney test. Lighter dots represent each indentation value and darker dots represent the median value per experiment. Graphs show median ± interquartile range. (**c**) Force-indentation AFM curves for vessel and bulk locations in 20µm-thick cryosections (n=40 pairs of bulk and vessel measurements from 4 brains). Graph shows median ± interquartile range. (**d**) Left: representative western blot of myosin-IIa expression in scramble control and myosin-IIa KO endothelial cells. Right: quantification of all western blots (one per experiment, 3 experiments). Graph shows mean ± standard deviation. (**e**) Force-indentation curves for scramble control and myosin-IIa KO endothelial cells (Scr: n=73, Myh9: n=60, 3 experiments). Graph shows median ± interquartile range. (**f**) Young's modulus of the collagen-HA gel mixture used in the microfluidic devices (n=81, 9 gels, 3 experiments). Lighter dots represent each indentation value and darker dots represent the median value per experiment. Graph shows median ± interquartile range. **g-l**, Dextran perfusions. (**g**) Proton NMR of dextran methacrylate, 70% degree of functionalization (calculated based on a previously published procedure, see methods). (**h**) Mean Young's modulus of perfused dextran gels for both soft and stiff gel formulations (n=3 perfusions). For each perfusion, a gel sample was kept for nanoindentation. Graph shows mean ± standard error of the mean. (**i**) Young's modulus of vessels in brain cryosections from perfusions in (h) measured with AFM (Soft: n=25, Stiff: n=21, 3 brains). Statistical analysis: two-sided T-test. Graph shows mean ± standard deviation. (**j**) Percentage of cells adhered to vessels after 24h of ex vivo culture in control, soft and stiff dextran brain slices (Control: n=11, Soft: n=11, Stiff: n=10, 3 experiments). Statistical analysis: one-way ANOVA test followed by a post hoc Tukey's test. Graphs show mean ± standard deviation. (**k**) Violin plots of invasion depths for cells moving through the bulk brain tissue after 24h of *ex vivo* culture in control, soft and stiff dextran brain slices (Control: n=517, 11 slices; Soft: n=727, 11 slices; Stiff: n=741, 10 slices; 3 experiments). (**l**) Violin plots of invasion depths for cells moving along the vasculature after 24h of *ex vivo* culture in control, soft and stiff dextran brain slices (Control: n=1349, 11 slices; Soft: n=1278, 11 slices; Stiff: n=1050, 10 slices, 3 experiments). (**m**) Mean Young's modulus of the stiff alginate gel formulation in (n) (n=3 experiments). Graph shows mean ± standard error of the mean. (**n**) Violin plots of cell velocities for cells migrating between alginate gels (Soft-Stiff: n=450, Stiff–Stiff: n=428, 4 experiments). The soft gel formulation was the same as in Fig. 5. For all violin plots, dots represent the median values per slice (k,l) or experiment (n). Statistical analysis: two-sided Mann–Whitney test or a Kruskal–Wallis test followed by a post hoc Dunn's test for multiple comparisons in k,l. Graphs show median ± interquartile range. For western blot quantification, protein expression was normalized to loading control (β-actin), and to the expression on the scramble control condition.

https://doi.org/10.1038/s41556-024-01532-6

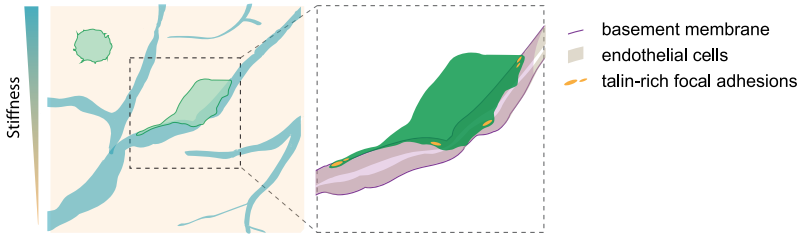

Extended Data Fig. 9 | Proposed model of vessel co-option. The differential stiffness between vessels and parenchyma promotes vessel co-option though a talin-dependent mechanism.

nature portfolio

Corresponding author(s): Christopher Chen

Last updated by author(s): Aug 26, 2024

Reporting Summary

Nature Portfolio wishes to improve the reproducibility of the work that we publish. This form provides structure for consistency and transparency in reporting. For further information on Nature Portfolio policies, see our Editorial Policies and the Editorial Policy Checklist.

Statistics

For all statistical analyses, confirm that the following items are present in the figure legend, table legend, main text, or Methods section.

n/a	Confirmed
☐	☒ The exact sample size (*n*) for each experimental group/condition, given as a discrete number and unit of measurement
☐	☒ A statement on whether measurements were taken from distinct samples or whether the same sample was measured repeatedly
☐	☒ The statistical test(s) used AND whether they are one- or two-sided *Only common tests should be described solely by name; describe more complex techniques in the Methods section.*
☒	☐ A description of all covariates tested
☐	☒ A description of any assumptions or corrections, such as tests of normality and adjustment for multiple comparisons
☐	☒ A full description of the statistical parameters including central tendency (e.g. means) or other basic estimates (e.g. regression coefficient) AND variation (e.g. standard deviation) or associated estimates of uncertainty (e.g. confidence intervals)
☐	☒ For null hypothesis testing, the test statistic (e.g. *F*, *t*, *r*) with confidence intervals, effect sizes, degrees of freedom and *P* value noted *Give P values as exact values whenever suitable.*
☒	☐ For Bayesian analysis, information on the choice of priors and Markov chain Monte Carlo settings
☒	☐ For hierarchical and complex designs, identification of the appropriate level for tests and full reporting of outcomes
☒	☐ Estimates of effect sizes (e.g. Cohen's *d*, Pearson's *r*), indicating how they were calculated

Our web collection on statistics for biologists contains articles on many of the points above.

Software and code

Policy information about availability of computer code

Data collection	MetaMorph (7.10.5.476) Las X (1.8.0.13370) Fusion (2.4.0.14) NIS-Elements (5.42.06) Optics11 Nanoindenter (V2.1.13) Asylum Research IgorPro MFP3D (16.10.211) JPK Data Processing software (v7.0.173)
Data analysis	Matlab (2022a/2023a) ImageJ (2.14.0/1.54f) Prism (GraphPad 10.0.3)

For manuscripts utilizing custom algorithms or software that are central to the research but not yet described in published literature, software must be made available to editors and reviewers. We strongly encourage code deposition in a community repository (e.g. GitHub). See the Nature Portfolio guidelines for submitting code & software for further information.

Data

Policy information about availability of data

All manuscripts must include a data availability statement. This statement should provide the following information, where applicable:

- Accession codes, unique identifiers, or web links for publicly available datasets
- A description of any restrictions on data availability
- For clinical datasets or third party data, please ensure that the statement adheres to our policy

Source data will be provided upon publication. All other data supporting the findings of this study are available from the corresponding author on reasonable request.

Research involving human participants, their data, or biological material

Policy information about studies with human participants or human data. See also policy information about sex, gender (identity/presentation), and sexual orientation and race, ethnicity and racism.

Reporting on sex and gender	Donor identity disguised.
Reporting on race, ethnicity, or other socially relevant groupings	Donor identity disguised.
Population characteristics	Donor identity disguised.
Recruitment	Boston Children's Hospital Blood Donation Center. All human donors provided informed consent, were not compensated, and their demographic information (sex, age, etc...) were not recorded.
Ethics oversight	Boston University IBC protocol: 18-1537.

Note that full information on the approval of the study protocol must also be provided in the manuscript.

Field-specific reporting

Please select the one below that is the best fit for your research. If you are not sure, read the appropriate sections before making your selection.

☒ Life sciences ☐ Behavioural & social sciences ☐ Ecological, evolutionary & environmental sciences

For a reference copy of the document with all sections, see nature.com/documents/nr-reporting-summary-flat.pdf

Life sciences study design

All studies must disclose on these points even when the disclosure is negative.

Sample size	No statistical test was used to determine sample size upfront. For the majority of the experiments a minimum of n=3 independent experiments were performed, with multiple measurements per experiment, which is sufficient to detect meaningful differences based on historical record with similar experiments.
Data exclusions	No data were excluded from the analyses.
Replication	All experiments were replicated independently at least three times except data for Extended Data Figure 2 i-k that was repeated two times.
Randomization	Animals were randomly assigned to each group. After tissue extraction, or for in-vitro experiments, randomization was not possible because groups were determined by the presence of a certain cell line, or device setup.
Blinding	Blinding was not possible as the same researcher executed and analyzed the experiments.

Reporting for specific materials, systems and methods

We require information from authors about some types of materials, experimental systems and methods used in many studies. Here, indicate whether each material, system or method listed is relevant to your study. If you are not sure if a list item applies to your research, read the appropriate section before selecting a response.

Materials & experimental systems

n/a	Involved in the study
☐	☒ Antibodies
☐	☒ Eukaryotic cell lines
☒	☐ Palaeontology and archaeology
☐	☒ Animals and other organisms
☒	☐ Clinical data
☒	☐ Dual use research of concern
☒	☐ Plants

Methods

n/a	Involved in the study
☒	☐ ChIP-seq
☒	☐ Flow cytometry
☒	☐ MRI-based neuroimaging

Antibodies

Antibodies used

For immunostaining, the primary antibodies used were laminin rabbit antibody (ab11575, Abcam; 1:1000 concentration for brain slices and 1:500 for devices), phospho-paxillin rabbit antibody (2541S, CellSignalling; 1:100 concentration) and anti-GFP chicken antibody (ab13970, 1:500 concentration, used for the B16-F10 cells). The secondary antibodies used were Alexa Fluor Plus 647 anti-rabbit (A32795, ThermoFisher; 1:500 concentration for laminin and 1:200 for p-paxillin) and Alexa Fluor Plus 488 anti-chicken (A32931, ThermoFisher; 1:500 concentration).
For western blots, the primary antibodies used were beta-actin rabbit antibody (4970S, CellSignalling; 1:5000 concentration), CD44 mouse antibody (3570T, CellSignalling; 1:1000 concentration), recombinant integrin beta1 antibody (ab134179, Abcam; 1:1000 concentration), zyxin rabbit antibody (PA5-78236, ThermoFisher; 1:1000 concentration), paxillin mouse antibody (AHO0492, ThermoFisher; 1:1000 concentration), talin1 mouse antibody (MCA4770GA, BioRad; 1:1000 concentration), talin2 mouse antibody (NBP2-50322, Novus; 1:1000 concentration) and vinculin mouse antibody (V9131, Sigma; 1:1000 concentration). The secondary antibodies used were anti-mouse HRP-linked antibody (7076S, CellSignalling; 1:1000 concentration) and anti-rabbit HRP-linked antibody (7074S, CellSignalling; 1:1000 concentration).

Validation

All antibodies were commercially available. The validation information for species and application can be found:

laminin (ab11575, Abcam): https://www.abcam.com/en-us/products/primary-antibodies/laminin-antibody-ab11575
phospho-paxillin (2541S, CellSignalling): https://www.cellsignal.com/products/primary-antibodies/phospho-paxillin-tyr118-antibody/2541?srsltid=AfmBOoqJ-s3mjImJnFoEiq6c6mMCcHPS0vx-H-XbZKWv6R8OpekH0WZt
anti-GFP chicken (ab13970, Abcam): https://www.abcam.com/en-us/products/primary-antibodies/gfp-antibody-ab13970
beta-actin (4970S, CellSignalling): https://www.cellsignal.com/products/primary-antibodies/b-actin-13e5-rabbit-mab/4970?srsltid=AfmBOorOLLAA4GNr_ANHkD8Mcka__U8A741XnSVLFylvzyshYrji_7JU
CD44 (3570T, CellSignalling): https://www.cellsignal.com/products/primary-antibodies/cd44-156-3c11-mouse-mab/3570?srsltid=AfmBOoqJWCwDoYeBI4LeNsFYI9vnoSYbiorV1X7z-Zff8tZuYhPZ7Oe9

integrin beta1 (ab134179, Abcam): https://www.abcam.com/en-us/products/primary-antibodies/integrin-beta-1-antibody-epr1040y-ab134179
zyxin (PA5-78236, ThermoFisher): https://www.thermofisher.com/antibody/product/Zyxin-Antibody-Polyclonal/PA5-78236
paxillin mouse antibody (AHO0492, ThermoFisher): https://www.thermofisher.com/antibody/product/Paxillin-Antibody-clone-5H11-Monoclonal/AHO0492
talin1 (MCA4770GA, BioRad): https://www.bio-rad-antibodies.com/monoclonal/human-talin-1-antibody-97h6-mca4770.html?f=purified
talin2 (NBP2-50322, Novus): https://www.novusbio.com/products/talin2-antibody-68e7_nbp2-50322
vinculin (V9131, Sigma): https://www.sigmaaldrich.com/US/en/product/sigma/v9131

Eukaryotic cell lines

Policy information about cell lines and Sex and Gender in Research

Cell line source(s)

1205Lu (gift from Rhoda Alani's lab, available from the Wistar Institute), WM983B (gift from Rhoda Alani's lab, available from Rockland), U2OS (gift from Clare Waterman's lab, available from ATCC), MCF7 (HTB-22, ATCC), MDA-MB-231 (HTB-26, ATCC), A375P (CRL-3224, ATCC), A375M2 (CRL-3223, ATCC), HEK-293T cells (632180, Clonetech), neonatal human dermal fibroblasts (nHDF, CC-2509, Lonza), MCF10A cells (CRL-10317, ATCC) , human brain vascular pericytes (HBVPC, 1200, ScienCell), primary human microvascular brain endothelial cells (HMBEC, ACBRI 376, CellSystems), NIH-3T3 mouse fibroblasts (CRL-1658, ATCC), B16-F10 (gift from Rhoda Alani's lab), EO771 (gift from Hadi Nia's lab, available from ATCC) and MDA-MB-231 derivative cell lines (MDA-MB-231 TGL, MDA-231-BoM-1833, MDA-231-BrM2-831, MDA-231-LM2-4175, Antibody and Bioresource Core Facility - MSKCC) were used in this study. T-cells were isolated from primary peripheral blood mononuclear cells (PBMC) obtained from whole peripheral blood from healthy donors at the Blood Donor Center at Boston Children's Hospital through a protocol approved by the Boston University Institutional Review Board (IRB).

Authentication

Cell lines used were not authenticated.

Mycoplasma contamination

All cell lines were tested negative for Mycoplasma.

Commonly misidentified lines
(See ICLAC register)

No commonly misidentified cell lines were used.

Animals and other research organisms

Policy information about studies involving animals; ARRIVE guidelines recommended for reporting animal research, and Sex and Gender in Research

Laboratory animals	In this study, we used 7- to 17-week-old mice from the FVB/NJ and STOCK Tg(TIE2GFP)287Sato/J strains (Jackson Laboratory) as well as 7-week-old nude mice (Taconic Biosciences). Animals were housed under 12 hours light/dark cycles, 68-79F temperatures and 30-70% humidity.
Wild animals	The study did not involve wild animals.
Reporting on sex	Both male and female mice were included in this study.
Field-collected samples	The study did not involve samples collected from the field.
Ethics oversight	All animal studies were approved and performed in accordance with guidelines of Boston University' Institutional Animal Care and Use Committees.

Note that full information on the approval of the study protocol must also be provided in the manuscript.